University of Alberta

Study of Enhanced Deposition due to Magnetic Field Alignment of Ellipsoid Particles Using Direct Numerical Simulations

by

Roberto Carlos Martinez

A thesis submitted to the Faculty of Graduate Studies and Research in partial fulfillment of the requirements for the degree of

Master of Science

Department of Mechanical Engineering

Fall 2012
Edmonton, Alberta

Abstract

A recent *in vitro* study demonstrated a non invasive method to enhance local deposition in a small airway by controlling the angular position of magnetic high aspect ratio particles. This technique could mitigate the challenge of providing sufficient therapeutic effects when using aerosolized chemotherapy techniques. To highlight the potential of this new magnetic field alignment approach the effect of increasing particle aspect ratio on the deposition efficiency was studied using direct numerical simulations. Simulations were done using an in house finite element algorithm. A steady air flow, typical of tidal breathing, was simulated through a three dimensional physiologically realistic bifurcation representing a single symmetrical bifurcation between generations 14 and 15 in the lung. For two different aspect ratios the deposition efficiency was found for the case of an unconstrained particle and magnetically aligned particle. Results indicate that forcing local alignment of high aspect ratio particles can increase local deposition considerably.

Acknowledgements

I would like to acknowledge the advice and guidance provided by Dr. Warren Finlay. I am also thankful for the the chance to learn a great deal from my fellow colleagues at the Aerosol Research Laboratory.

More importantly I would like to thank my parents (Carlos and Genny), my siblings (Fernando and Adriana) and my fiancé (Taylor Roy) for supporting and encouraging me throughout this degree. Everything I have accomplished is due to the support and love I have received from these important people.

Table of Contents

1 Introduction **1**

1.1 Pharmaceutical Aerosols and Localized Drug Targeting 1

1.2 Particle Deposition Models 5

1.3 Summary of Thesis 7

2 Background **9**

2.0.1 Lung Geometry and Models 9

2.1 Particle Behaviour in the Lung 12

2.2 Magnetic Alignment of High Aspect Ratio Particle 15

2.3 Analytical Deposition Equations 19

2.3.1 Sedimentation 19

2.3.2 Impaction and Interception 21

3 Method and Theory **25**

3.1 Governing Equations 25

3.1.1 Fictitious Domain Method 27

3.2 Geometry Generation 29

3.3 Bifurcation Mesh Generation 29
3.4 Steady Air Flow Analysis 31
3.4.1 Simulation Conditions 31
3.4.2 Inlet Boundary Conditions 32
3.4.3 Outlet Boundary Conditions 32
3.4.4 Bifurcation Wall Boundary Condition 33
3.4.5 Flow Pattern Analysis 33
3.5 Particle Trajectory Simulations 34
3.5.1 Particle Geometry 34
3.5.2 Micro Grid Geometry and Mesh Generation 34
3.5.3 Effect of Particle Time Step 35
3.5.4 Effect of Micro Grid Size and Spacing 35
3.5.5 Effect of Solver Convergence Criterion 36
3.5.6 Computational Equipment and Simulation Run Time . 36
3.6 Deposition Simulations 36
3.6.1 Deposition Efficiency Calculation 36
3.6.2 Deposition Efficiency: Strong Streamline Alignment Case 39
3.6.3 Deposition Efficiency: Magnetically Aligned Case . . . 40
3.7 Theoretical Deposition Calculations 40

4 Results **42**

4.1 Steady Flow Field 42
4.2 Particle Simulation Sensitivity Analysis 45

4.3 Deposition Efficiency 47
4.4 Theoretical Deposition Results 51

5 Discussion **54**
5.1 Steady Flow Field 54
5.2 Particle Simulation Sensitivity Analysis 55
5.3 Deposition Efficiency 56
5.4 Deposition Enhancement 60

6 Conclusion **61**

Bibliography **63**

A Double Bifurcation **72**
A.1 Method 72
A.1.1 Geometry Generation 72
A.1.2 Inlet Boundary Conditions 74
A.1.3 Outlet Boundary Conditions 74
A.1.4 Bifurcation Wall Boundary Condition 75
A.1.5 Flow Pattern Analysis 75
A.2 Double Bifurcation Steady Flow Results 76
A.3 Discussion 76

B Spherical Particle Validation **78**
B.1 Method 78

B.1.1 Bifurcation Geometry and Mesh Generation 78
B.1.2 CFX Solver 79
B.1.3 Flow and Boundary Conditions 79
B.1.4 Convergence Criteria 81
B.1.5 Effect of Particle Time Step on Deposition 81
B.1.6 Mesh Convergence of Deposition 81
B.1.7 CFX Validation of FDM Code 81
B.2 Results 82
B.2.1 Effect of Time Step and Grid 82
B.2.2 Spherical Particle Trajectory Comparison Between the CFX and FDM Result 83
B.3 Discussion 84

List of Tables

3.1 Summary of single bifurcation dimensions in millimeters . . . 29

4.1 Results of grid convergence index (GCI) analysis completed on the macro grid representing the steady flow through the small bifurcation model. Here, r is the refinement factor, ϵ_{rms} is the rms error and the GCI is the grid convergence index (Celik et al., 2008) 45

4.2 Change in angular position of the maximum and minimum angular velocity of the particle occurring with different dimensionless time steps 46

4.3 Deposition efficiency results based on the inlet deposition boundary for each case and aspect ratio. The deposition boundary error is the difference between the deposition efficiency given by the deposition region of particles that deposited and the deposition boundary of particles that did not deposit. 50

4.4 Deposition enhancement between Case [1] and Case [2] for both aspect ratio 6 and 20 51

4.5 Theoretical deposition probabilities due to sedimentation, impaction and interception for each Case and aspect ratio combination. The lower and upper range for the impaction probability is due to two different methods used. 52

4.6 Absolute and relative difference between the theoretical total deposition and the numerically calculated total deposition. . . 53

A.1 Summary of double bifurcation dimensions in mm 73

B.1 The relationship between the "regional" deposition and time step for both the coarse and refined grid. Also given is the absolute and relative difference between the results given by the coarse and refined grid. 83

B.2 Final position results using CFX and the fictitious domain method (FDM). The initial position of the spherical particle was x = 2.20E-5 and z = 1.26E-3. 84

B.3 Final position results using CFX and the fictitious domain method. The initial position of the spherical particle was x = 2.40E-5 and z = 2.45E-3. 84

List of Figures

1.1 A schematic showing the change in angular position of magnetically susceptible high aspect ratio particles when a magnetic field is introduced. Green zone represents the magnetic field. High aspect ratio particles within magnetic field align with the magnetic field. Particles outside magnetic field tend to align parallel to direction of the local flow in the lung bifurcation. 5

2.1 Schematic of symmetrical morphologically realistic bifurcation (MRB) model given by Hegedűs et al. (2004) and all applicable parameters. 11

2.2 Ratio between the magnetic torque and the aerodynamic torque for a composite particle immersed in both a magnetic field and shear as a function of the magnetic angle ϕ. The magnetic torque was calculated using the equations given by Skomski et al. (2007) and Shine and Armstrong (1987). The velocity gradient, saturation magnetization and Beta values were 813 s^{-1}, 4.7 x 10^5 A/m and 20 respectively. 18

2.3 Ratio between the magnetic torque and the aerodynamic torque for a composite particle immersed in both a magnetic field and shear as a function of the magnetic angle ϕ. The magnetic torque was calculated using the equations for the combined magnetic field of two dipoles and the torque equation given by Shine and Armstrong (1987). The velocity gradient, saturation magnetization and Beta values were 813 s^{-1}, 4.7 x 10^5 A/m and 20 respectively. 19

3.1 Single Bifurcation Geometry 30

3.2 Schematic of micro grid geometry consisting of three separate control shapes. Different grid spacing was used within the rectangular box, cylinder and ellipsoid. 35

3.3 Schematic of how the "deposition" area is defined 38

4.1 Air velocity profile of inspiratory flow through the small bifurcation model. Velocity profiles are from cuts at the center of the bifurcation in two different planes A) y-x plane B) y-z plane . 43

4.2 Axial velocity profile along the line D-D$'$ seen in Figure 4.1 . . 44

4.3 Case [1] and Case[2] isolated deposition regions at the bifurcation inlet for a particle with an aspect ratio of 6. Deposition boundary lines represent the division where the particles entering to the left deposit and those to the right do not deposit. The x and z position correspond to the axes located at the center of the inlet seen previously in Figure 3.3. The x and z position were normalized by dividing the dimensionless position by the length of a particle with an aspect ratio of 6. The bifurcation inlet wall is the outer limit boundary of the fluid domain at the inlet. 48

4.4 Case [1] and Case[2] isolated deposition regions at the bifurcation inlet for a particle with an aspect ratio of 20. Deposition boundary lines represent the division where the particles entering to the left deposit and those to the right do not deposit. The x and z position correspond to the axes located at the center of the inlet seen previously in Figure 3.3. The x and z position were normalized by dividing the dimensionless position by the length of a particle with an aspect ratio of 6. The bifurcation inlet wall is the outer limit boundary of the fluid domain at the inlet. 49

A.1 Double bifurcation geometry **A.** Parent and daughter in same vertical plane **B.** Parent and daughter in in a 90 degree plane 73

A.2 Double bifurcation velocity profile at the inlet of the single bifurcation 77

Chapter 1

Introduction

1.1 Pharmaceutical Aerosols and Localized Drug Targeting

Inhalation therapy has become well known in its use to treat lung disease such as asthma, chronic obstructive pulmonary disease, cystic fibrosis(Finlay et al., 2000), and chronic pulmonary infections(Golshahi et al., 2008) but more recently there have been new developments in the inhalation treatment of lung cancer. The American Cancer Society (2011) are estimating about 1.6 million new cancer cases for 2011 to be added to the already 11.7 million (as of 2007) of people already affected by cancer. Lung cancer will account for 14% of these newly diagnosed persons (American Cancer Society, 2011), while in Canada it accounts for 27% of deaths due to cancer (Canadian Cancer Society, 2011). Inhalation chemotherapy holds some advantages in comparison to established forms of treatment such as intravenous (IV) therapy. Inhalation chemotherapy has been shown to provide equal therapeutic effects as the more commonly used method of IV administration but with reduced systemic side effects(Wittgen et al., 2007; Otterson et al., 2007; Gagnadoux et al., 2005). Aerosol therapy has the advantage of convenience

over IV therapy which is important for chemotherapeutic agents where efficacy of the treatment is highly dependent on the administration schedule (Reddy and Couvreur, 2008).

The problem all inhalation therapies involving aggressive medicine suffer from is staying within dose limiting toxicity levels. Otterson et al. (2007) found that Doxorubicin (a chemotherapeutic agent) reached the safe dose limit before it could provide sufficient effect to be used as the sole treatment. Currently inhalation chemotherapy is considered as an important adjuvant to current treatment techniques (Wiedmann and Yi, 2010). Improving drug delivery by targeting drug delivery where it is most effective would help alleviate this problem. In the case of inhalation chemotherapy, deposition could be targeted to the site of the tumor or for systemic therapy the alveolar airways would be targeted as this is where the gas exchange with the blood stream occurs.

There are many forms of targeted drug delivery with the simplest form of targeting being a mechanistic approach. This includes controlling parameters such as particle characteristics, inhalation waveform, particle concentration and particle release positions (Kleinstreuer et al., 2008). Except this type of targeting is very limited to targeting to a broad range of regions in the lungs. For greater isolation other methods such as chemoembolization and isolated lung perfusion exist but are considered extremely invasive techniques (Bar et al., 2009). These surgical techniques also require the patient to be in the condition to allow for such an invasive technique. Magnetic targeting has been studied as a possible form of non invasive targeting. Dames et al. (2007) studied the use of a magnetic targeting method where deposition enhancement is encouraged by employing a magnetic field to change the

trajectory of aerosol droplets containing superparamagnetic iron oxide nanoparticles. The change in translational position of the particles is related to the magnetic field gradient and unfortunately the magnetic field gradient decreases dramatically with the distance from the magnetic field source. Considering the dimensions of typical human lungs, until new magnetic field generating designs are made this type of targeting method is limited (Bar et al., 2009).

Recently Martin and Finlay (2008b) have developed a form of magnetic targeting that does not suffer from the magnetic gradient limitation. Deposition is encouraged by controlling the angular position of high aspect ratio particles in order to increase deposition due to interception. High aspect ratio particles (elongated particles or fiber like particles) in the lungs tend to spend most of their travel time with their longer axis aligned to the direction of the flow (Jeffery, 1922). Thus these high aspect ratio particles have aerodynamic properties equivalent to that of smaller spherical particles. This is advantageous in terms of being able to penetrate into the distal airways with an increase in drug dosage when compared to a spherical particle. Figure 1.1 shows a schematic of how the magnet targeting method would work in a small bifurcation in the lung. Martin and Finlay (2008c) theoretically proved that the resulting magnetic torque on a high aspect ratio particle seeded with ferromagnetic particles could be capable of overcoming the hydrodynamic torque experienced by the particle. The theory was then validated by demonstrating the difference in angular position of particles on membrane filter with and without a magnetic field (Martin and Finlay, 2008a). Scanning electron microscope of the filter demonstrated how the particles deposited where aligned to the external magnetic field. Finally an *in vitro* study was completed where deposition of high aspect ratio particles were recorded in a small

bifurcation model with and without a magnetic field(Martin and Finlay, 2008b). For a polydispersed aerosol the deposition in the small bifurcation model increased by a factor of 1.7 when the external magnetic field was applied. More recently an in vivo study was done by Redman et al. (2010)using the magnetic alignment technique to enhance deposition in rabbits. The magnetic targeting technique resulted in enhanced deposition in the basal and distal airways in the lungs of the rabbits.

These studies have demonstrated that there is potential to use the magnetic targeting technique to enhance local deposition. This technique could be used to enhance deposition in the unhealthy lobe and thus decrease side effects in the healthy lobe. With an increase in drug delivery efficacy to the sites of interest there would be an increase in therapeutic effects without having to suffer from an increase in side effects. This would allow for effective use of aggressive medicine such as chemotherapeutic agents without reaching dose limiting toxicities. One of the most important parameters is the aspect ratio of the particle since interception is highly dependent on the length of the particle. Thus the end goal of this study is to use numerical methods to quantify the relationship between the deposition enhancement and the particle's aspect ratio.

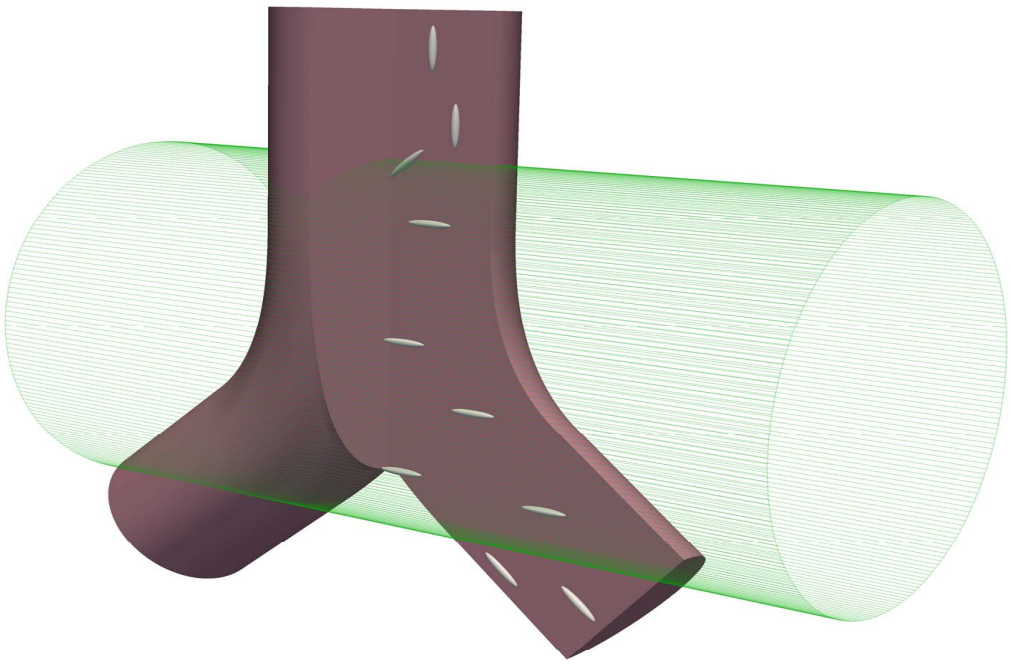

Figure 1.1: A schematic showing the change in angular position of magnetically susceptible high aspect ratio particles when a magnetic field is introduced. Green zone represents the magnetic field. High aspect ratio particles within magnetic field align with the magnetic field. Particles outside magnetic field tend to align parallel to direction of the local flow in the lung bifurcation.

1.2 Particle Deposition Models

A numerical approach was deemed appropriate due to the difficulty of precisely controlling the different parameters in the experimental results. In the work done by Martin and Finlay (2008b) and Redman et al. (2010) polydispersed

aerosols were used and deposition was based on mass deposited. Therefore it is difficult to quantify which size range contributed most significantly to the local deposition enhancement. The use of numerical methods would give insight into the trajectories of the particles when the particle has a fixed angular position, something that would not normally be possible. To accomplish this it would take a numerical method capable of accurately simulating the trajectory of high aspect ratio particles through a three dimensional bifurcation model.

Information on the deposition of fibers in the lung is limited compared to the deposition of spherical particles and this is reflected in current computational and theoretical methods. Since it is widely accepted that high aspect ratio particles tend to spend most of their time aligned to streamlines, many theoretical fiber deposition models rely on substituting an equivalent spherical diameter with already established spherical deposition equations (Harris and Fraser, 1976; Yu et al., 1986). Numerical studies on fibers base the particle equations of motion on equivalent diameter theory (Hofmann et al., 2005) or on past theoretical fiber motion results (Zhang et al., 1996). Hofmann et al. (2005) used this concept with the addition of interception to study the deposition of fibers in a third generation lung successfully. Their results validated the idea that spherical approximations may be reasonable for high shear flow (Broday et al., 1998). Although interception was incorporated into the study they found that it did not contribute significantly. The FIBROS program developed by Sturm and Hofmann (2009) uses a compilation of empirical and analytical equations to calculate deposition of fibers in the different generations of the lung. This model relies on equations that have been adapted from spherical particles to be used with fibers. This program

also does not allow for the particle's angular position to be fixed. Many of the above numerical studies focus on fiber deposition in the upper conducting airways but interception does not play a significant role in these areas. Therefore the importance of interception deposition has never been the main focus of past studies. To the author's knowledge, allowing for a fixed angular position in order to study its effect on deposition has never been done. In the present work the opportunity has been given to use a fictitious domain algorithm capable of all the necessary simulations options needed to complete such a study. The most recent version of the algorithm was used to study the effect of particle shape on its angular movement in shear flow Roshchenko et al. (2011a). The algorithm is described in more detail in Section 2.3.2.

1.3 Summary of Thesis

The goal of this study was to use a direct numerical algorithm to study the trajectory of high aspect ratio particles in a small bifurcation model while controlling the particle's angular position. The particle trajectories were then used to estimate the deposition with and without magnetic field alignment. The ratio between the two cases is considered the deposition enhancement factor. This was completed for a particle aspect ratio of 6 and 20 in order to quantify the effect of the particle aspect ratio on the deposition enhancement factor. The first component of the model was to simulate the flow of air through a small bifurcating airway representing generation 14 of the lung. Following the simulation of the flow field, a sensitivity analysis was completed on the particle trajectories. Finally simulations were completed to find the deposition estimates. Chapter 2 introduces theory on lung geometry,

particle behavior and particle deposition models. Chapter 3 describes the method used for both the flow field simulations and the particle simulations. Results from the study are given in Chapter 4, followed by a discussion in Chapter 5. Chapter 6 summarizes the work completed.

Chapter 2

Background

2.0.1 Lung Geometry and Models

The lung is made up of an intricate set of bifurcating tubes, starting with the trachea which is located after the extrathoriac region (made up of the nasal cavity, oral cavity, pharynx and larynx). From the trachea begins the tracheo-bronchial region which leads into the gas exchange area of the lung known as the alveolar or pulmonary region. Each sequential bifurcating airway is assigned a generation number with the trachea being generation zero. Due to the changes in physical characteristics and flow conditions as one moves through the different generations most studies focus on a single bifurcation or set of bifurcations representing the generations of interest. These bifurcations are typically modeled using one of two methods. The first method is the use of 3-D imaging, for example the use of computed tomography (CT) images of human airway casts or a patient's lung. The use of 3-D imaging may provide detailed data that can be helpful in studying inter subject variability or the effect of specific morphological features (De Backer et al., 2008). From a numerical stand point the use of 3-D imaging models can introduce complexities in the grid generation process and may require

modifications in the model before it can be used (Choi et al., 2007). Thus the use of idealized geometries has grown to be widely accepted. An idealized geometry is typically created by inputting accepted morphological parameter values into a mathematical model describing the bifurcation geometry. The mathematical descriptions of the bifurcation surface typically separate the bifurcation into three different regions. The parent tube, daughter tubes and the transition zone which connects the former two regions and includes the carinal ridge. How the transition zone is described is what differentiates the different mathematical models. Earlier models like the "narrow" and "wide" model (Balásházy and Hofmann, 1993; Balásházy, 1994) represent the outer surface of the transition zone using straight lines connecting the parent and daughter airways and a sharp wedge shape for the carina. A more complex and realistic description is the physiologically realistic bifurcation (PRB) model by Heistracher and Hofmann (1995). Balásházy et al. (1996) showed how the PRB model can better represent the flow pattern and particle deposition than the "wide" or "narrow" model. The morphologically realistic bifurcation (MRB) was then created by Hegedűs et al. (2004) by fixing some mathematical problems experienced when trying to create the PRB model. More importantly Hegedűs et al. (2004) showed that computer aided design (CAD) software could be used to accurately create the bifurcation model. Figure 2.1 shows a symmetrical MRB model and the following parameters R_c, R^*, ϕ, L', and D which represent the radius of carina roundness, curvature radius, branching angle, cylindrical length, and diameter. The parent region is made up of a straight cylindrical portion of length L'_p and diameter D_p. Two narrowing tubes following a curve with a radius of curvature R^* and a bifurcation angle of ϕ, is considered the transition region. The two daughter

regions are straight cylindrical tubes.

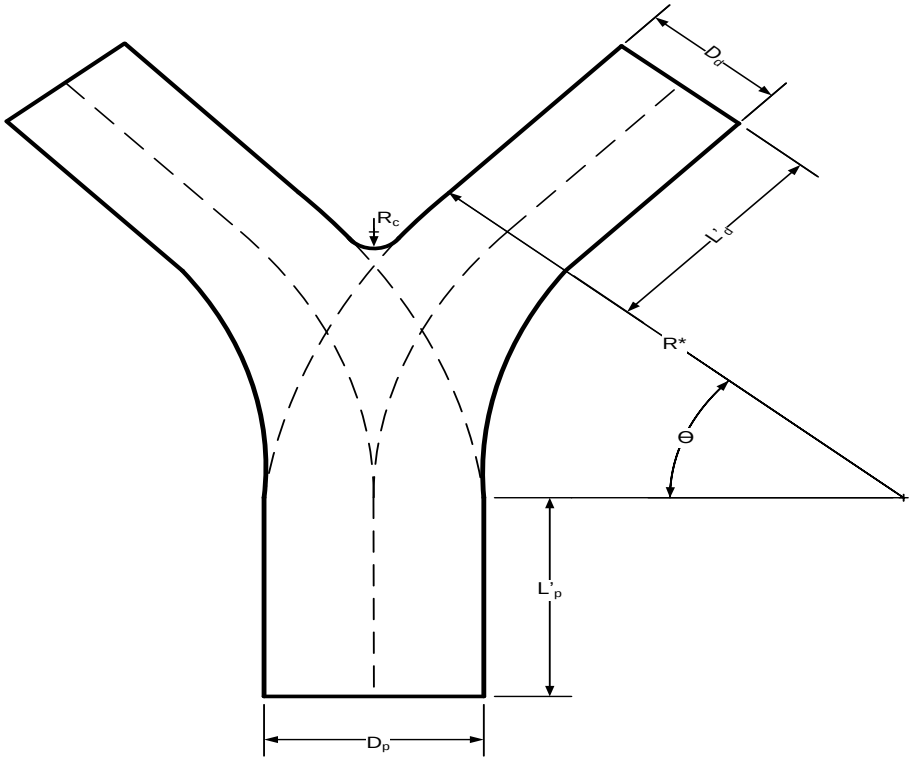

Figure 2.1: Schematic of symmetrical morphologically realistic bifurcation (MRB) model given by Hegedűs et al. (2004) and all applicable parameters.

The length and diameters of each generation can be taken from the model created by Finlay et al. (2000) who combined the results from several studies (Phillips et al., 1994; Haefeli-bleuer and Weibel, 1988; Weibel, 1963) to create a more accurate model. The lengths given by Finlay et al. (2000) corresponds to the total length of each generation, therefore some calculations must be completed before finding the daughter and parent lengths seen in Figure 2.1. Hegedűs et al. (2004) gave the following equations

$$L'_p = 0.8L_p \tag{2.1}$$

$$L'_d = 0.2L_d + L_d - \phi R^* \tag{2.2}$$

L_p and L_d are the parent and daughter portions that include both the straight and transitional portion of the bifurcation. Therefore to find the lengths for a single a bifurcation Equations 2.1 and 2.2 can be calculate over three consecutive bifurcations using the values given by Finlay et al. (2000). The radius of curvature and carina radius for a normal human bronchial tree was given by Horsefield et al. (1971) as

$$1 < \frac{R^*}{D_p} < 0.1 for D_p < 1.5mm \tag{2.3}$$

$$\frac{R_c}{D_p} < 0.1 \tag{2.4}$$

The carina radius given by Horsefield et al. (1971) was verified by Olson and Hammersley (1992) when studying small airway casts with diameters less than 0.1 mm. Both Horsefield et al. (1971) and Olson and Hammersley (1992) give the average bifurcation angle as 50^o. With the above reference geometries and the steps given by Hegedűs et al. (2004) a morphologically realistic bifurcation can be created.

2.1 Particle Behaviour in the Lung

To better understand the magnetic targeting method it is important to review the behavior of high aspect ratio particles in the lungs. The work done by

Jeffery (1922) on the behavior of ellipsoid particles in linear shear flow is considered to be a good representation of the behavior of high aspect ratio particles in the lungs. For a neutrally buoyant solid ellipsoid particle, Jeffery (1922) was able to define an equation for the hydrodynamic torque on a neutrally buoyant solid ellipsoid particle

$$T_a = 2\pi\mu G d_e^2 l_e \left(\frac{d_e^2 \cos^2\phi + l_e^2 \sin^2\phi}{3\left(d_e^2\beta_o + l_e^2\gamma\right)} \right) \tag{2.5}$$

where ϕ, G, d_e, and l_e are the angular position, velocity gradient, ellipsoid diameter, and ellipsoid length respectively. An angular position of 0 and 90 degrees corresponds to when the particle's major axis is parallel and perpendicular to fluid flow respectively. Jeffery (1922) was also able to show that an ellipsoidal particle exhibits a periodic rotation (referred to as Jeffery's orbit) around the axis normal to the velocity gradient plane. The angular velocity associated with Jeffery's orbit is given by

$$\frac{d\phi}{dt} = G\frac{d_e^2 \cos^2(\phi) + l_e^2 \sin^2(\phi)}{d_e^2 + l_e^2} \tag{2.6}$$

The max and min value of the angular velocity from Equation 2.6 occurs when the particle angular position is 0 and 90 degrees respectively. This suggests that during its rotation the particle spends most of its time with its major axis parallel to the fluid flow. The scenario of the particle spending most of its time parallel to the linear velocity profile is one limiting case. The other limiting case occurs with major axis initially positioned perpendicular to the linear velocity profile and the particle exhibits a rolling motion. This is due to the fact that the fluid inertia terms were ignored in the analysis. Subramanian and Koch (2005) extended the analysis done by Jeffery (1922)

by including the fluid inertia terms. Including the fluid inertia, they showed that the particle's major axis will tend to drift toward being parallel to the velocity gradient plane.

During the derivation of Jeffery's orbit the particle was assumed to be neutrally buoyant. This is typically untrue in pharmaceutical aerosols where particles are thousand times denser than air. Asgharian and Anjilvel (1995) studied how the effect of the particle inertia can affect the particle orientation described by Jeffery (1922). What they found is that the effect of the inertia is a function of the particle aspect ratio and a non-dimensional parameter, κ given by

$$\kappa = \frac{\rho_e G d_e^2}{\mu} \tag{2.7}$$

Asgharian and Anjilvel (1995) showed how the period of rotation of the ellipsoid changed with κ when compared to the period of rotation without the particle inertia. This result showed that at lower values of κ the period of rotation agreed well with that derived from Jeffery's analysis. On the other hand with increasing values of κ the period of rotation decreased reaching a minimum level before increasing. The ranges of κ where the period of rotation is not affected by the particle's density is dependent on the aspect ratio of the particle. For particles with an aspect ratio between 5 and 20 a value of κ less than one would be within the range where the particle inertia does not affect its period of rotation. To gauge the importance of the particle inertia the value of κ can be calculated for a ellipsoid particle with a diameter 0.5 μm and density of 1190 kg/m^3 and with a velocity gradient seen near the wall in a generation 14 bifurcation. The value of κ for these parameters is much

lower than 1. The alignment behavior of fibers was validated experimentally by Ding et al. (1993) who showed the alignment of the ellipsoid particles in the direction of the streamlines of a bifurcating tube. With respect to high aspect ratio particles in the lungs, the findings by Jeffery (1922) means the particles will travel with their major axis aligned to the direction of the streamlines. This is beneficial in that it allows high aspect ratio particles to have the aerodynamic properties of smaller spherical particles but the benefit of more mass. The particle's tendency to align to the streamlines decreases the probability of interception. The magnetic targeting method by Martin and Finlay (2008b) changes the particle's angular position in order to increase the probability of interception and thus enhance local deposition.

2.2 Magnetic Alignment of High Aspect Ratio Particle

The theory and method of the magnetic targeting method has been discussed in great detail in previous works; a brief description is given here with an emphasis on the components that are pertinent to the computational method used in this study. Shine and Armstrong (1987) gave the following equation for the magnetic torque on an ellipsoid particle

$$\vec{T_m} = \mu_o \int \left(\vec{M} \times \vec{H} \right) dV \tag{2.8}$$

The magnetic torque is a function of the magnetic gradient and field strength reperesented by M and H respectively. Typical pharmaceutical aerosols are not inherently magnetic but their magnetic susceptibility can be altered by seeding magnetic nanoparticles onto the aerosol drug particle. Using a permanent magnet, Martin and Finlay (2008a) where able to show

the alignment of particles composed of non magnetic material coated with a magnetic material. For the case where a non magnetic material and magnetic material are combined the magnetization can be described by the equation given by Skomski et al. (2007)

$$M_p = f_m M_m \tag{2.9}$$

where M_p and M_m are the magnetization of the combined material and the magnetic particles respectively. Then f_m is the volume fraction made up of the magnetic material. Skomski et al. (2007) also gave the demagnetization factor for a composite material as

$$D_p = D_m(1 - f_m) + D_c f_m \tag{2.10}$$

where D_m and D_c are the demagnetization factor for the magnetic and carrier particle respectively. These two equations above can be substituted into the torque equation given by Shine and Armstrong (1987). This results in the following equation

$$T_m = \mu_o M_s^2 V (D_{min} - D_{maj}) \sin\Phi \cos\Phi \tag{2.11}$$

where M_s is the saturation magnetization and V is the volume of the ellipsoid. D_{min} and D_{maj} are the demagnetization factors along the minor and major axis of the particle. The angle between the ellipsoid's major axis and the saturating magnetic field is represented by Φ. Martin and Finlay (2008c) point out that the above approach does not take into account that the surface of the carrier particle is not completely covered by the

magnetic particles. Martin and Finlay (2008c) found Equation 2.12 by instead modeling the composite particle as a carrier particle with a row of spherical ideal dipoles embedded along the major axis of the carrier particle.

$$T_m = \mu_o V H M \left(\frac{d_m}{L_{spacing}} \right)^3 \sin\Phi \cos\Phi \tag{2.12}$$

where M is the magnetization of the magnetic particle modeled by the dipole, d_m is the diameter of the magnetic particles and $L_{spacing}$ is the spacing between the centers of the neighboring particles. Using Equation 2.11 and Equation 2.12, Martin and Finlay (2008c) were able to show that the maximum magnetic torque is greater than the maximum aerodynamic torque typically found in the bronchioles of the lung. During the magnetic alignment of the particles there is an assumption that the particles align with the magnetic field and at this point the magnetic torque is at its minimum. Therefore in reality the angular position of the magnetically aligned particle would be where the magnetic torque and aerodynamic torque are equal. Using the same typical magnetic values given by Martin and Finlay (2008c) and the flow rate conditions in a generation 14 bifurcation, the ratio between the aerodynamic and magnetic torque can be calculated with respect to, Φ. Figure 2.2 shows that the magnetic torque calculated using the equations given by Shine and Armstrong (1987) is much larger for all values of f_m. At angle Φ of 1^o the magnetic torque is over one hundred times greater than the aerodynamic torque. Figure 2.3 shows that for the most part the magnetic torque will be greater than the aerodynamic torque at low values of Φ. The only exception may be for a $d_m/L_{spacing}$ value of 0.05 but even in that case the particle need only change in angle by less than 5^o before the magnetic torque

is again larger than the aerodynamic torque. This analysis was also done for a shear gradient seen in the parent tube. Even if the velocity gradient is larger in the daughter tube the aerodynamic torque would not be at its maximum because the magnetic field, and therefore the particle orientation, is no longer perpendicular to the flow. Based on the above considerations the assumption that the particle angular position is constant when immersed in a magnetic field should be valid under the conditions seen in this study.

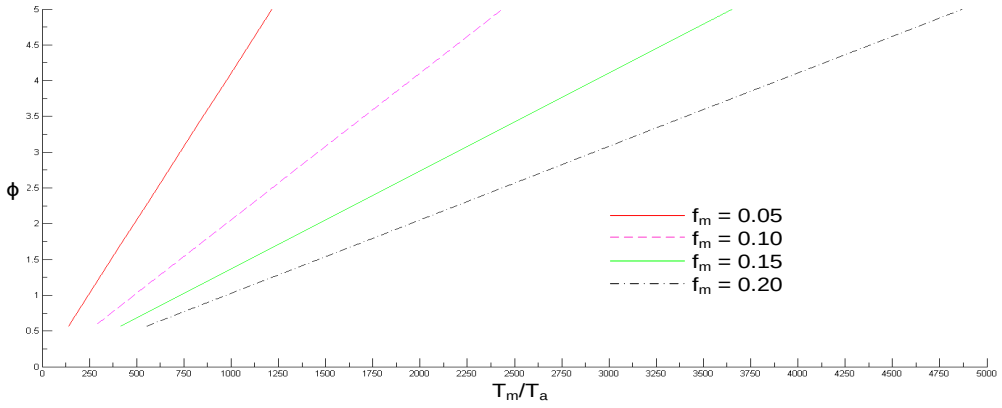

Figure 2.2: Ratio between the magnetic torque and the aerodynamic torque for a composite particle immersed in both a magnetic field and shear as a function of the magnetic angle ϕ. The magnetic torque was calculated using the equations given by Skomski et al. (2007) and Shine and Armstrong (1987). The velocity gradient, saturation magnetization and Beta values were 813 s^{-1}, 4.7 x 10^5 A/m and 20 respectively.

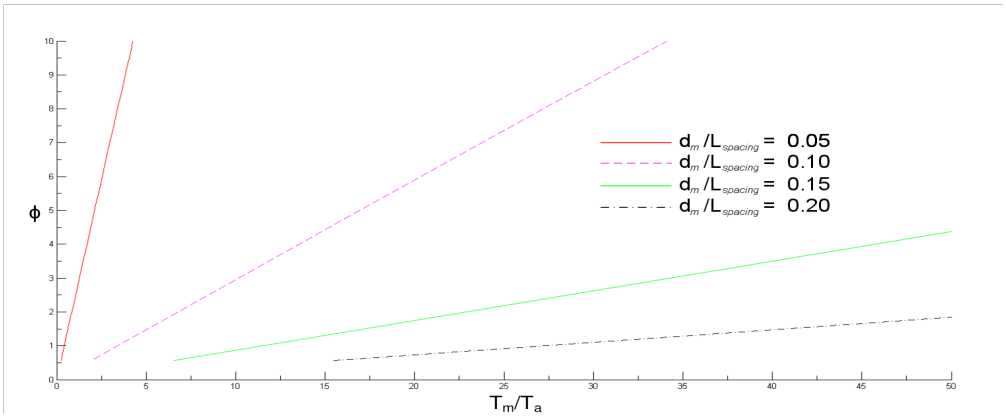

Figure 2.3: Ratio between the magnetic torque and the aerodynamic torque for a composite particle immersed in both a magnetic field and shear as a function of the magnetic angle ϕ. The magnetic torque was calculated using the equations for the combined magnetic field of two dipoles and the torque equation given by Shine and Armstrong (1987). The velocity gradient, saturation magnetization and Beta values were 813 s^{-1}, 4.7 x 10^5 A/m and 20 respectively.

2.3 Analytical Deposition Equations

This section gives an overview of the theory behind the analytical equations used to determine deposition efficiency of a fiber. These analytical equations can be broken down into the following different deposition mechanisms of diffusion, sedimentation, impaction and interception.

2.3.1 Sedimentation

To predict the amount of deposition due to sedimentation the analytical model given by Heyder and Gebhart (1977) can be used. The analytical model gives the deposition of particles due to gravity in an inclined circular

tube with a Poiseuille flow profile. The deposition efficiency is given as

$$\eta_s = \frac{2}{\pi}\left[2\kappa_s\sqrt{1-\kappa_s^{2/3}} - \kappa_s^{1/3}\sqrt{1-\kappa_s^{2/3}} + arcsin(\kappa_s^{1/3})\right] \tag{2.13}$$

where

$$\kappa_s = \frac{3\nu_s L cos\Theta}{4UD} \tag{2.14}$$

L, D, ν_s, U, and Θ are the tube length, tube diameter, particle settling velocity, average velocity and the angle of inclination with respect to gravity. For Equation 2.13 to be used, the following condition must be satisfied, $\nu_s \sin\Theta/U << 1$. For the conditions of interest in this study this restriction is shown to be satisfied later in the Results section. Heyder and Gebhart (1977) validated this analytical equation by comparing to their experimental results. The settling velocity in Equation 2.14 can be derived by equating the gravity force and drag force experienced by an ellipsoid particle. For a prolate ellipsoid in Stokes flow this settling velocity is given as

$$\nu_s = \frac{d_f^2 \beta g \rho_f}{18\mu\chi_s} \tag{2.15}$$

Here, g and χ represent gravity and a sedimentation shape factor respectively. Oseen (1927) determined the shape factor corresponding to a particle in motion perpendicular and parallel to its major axis. Both shape factors are given below

$$\chi_{s\perp} = \frac{8\left(\beta^2-1\right)}{3\left[\frac{2\beta^2-3}{\sqrt{\beta^2-1}} ln\left(\beta+\sqrt{\beta^2-1}\right)+\beta\right]} \tag{2.16}$$

$$\chi_{s\parallel} = \frac{4\left(\beta^2-1\right)}{3\left[\frac{2\beta^2-1}{\sqrt{\beta^2-1}} ln\left(\beta+\sqrt{\beta^2-1}\right)-\beta\right]} \tag{2.17}$$

2.3.2 Impaction and Interception

Cai and Yu (1988) gave deposition probabilities for an ellipsoid particle due impaction and deposition. Their analysis is based on the stopping distance of a particle. The stopping distance is defined as

$$s = Cv_p\tau\left(1-e^{\frac{-1}{\tau}}\right) \tag{2.18}$$

where C, v_p, τ are the Cunningham slip factor, particle velocity and relaxation factor. The relaxation factor is defined below

$$\tau = \frac{\rho_p d_p^2}{18\mu} \tag{2.19}$$

Using the stopping distance, a deposition region is identified at a cross section through the bifurcation near carina. Anything within the stopping distance away from the inner wall is assumed to deposit due to impaction. Deposition due to interception is included by extending the deposition region by a constant interception distance. Assuming a uniform particle concentration, the deposition efficiency is the ratio between deposition region flow rate and the total flow rate. Cai and Yu (1988) used this method to develop deposition efficiency equations for three different particle angular positions, 1) the major axis of the particle is aligned to the daughter tube, 2) the major

axis of the particle stays aligned parallel to the inlet, 3) the major axis of the particle is at a random orientation. The first case represents strong particle alignment and therefore an interception term is not included. The second case represents a particle with high inertia and the third case represents the effect of mixing due to secondary flow. Cai and Yu (1988) gave Equation 2.20 and Equation 2.21 below to calculate the deposition efficiency corresponding to case 1 and case 3 respectively.

$$\eta = G(\alpha, R_d/R_p)(St)_{f_1} \tag{2.20}$$

$$\eta = G(\alpha, R_d/R_p)(St)_{f_3} + I_3(\alpha, R_d/R_p) l_e/R_d \tag{2.21}$$

The first and second term in Equation 2.21 represent the deposition efficiency due to impaction and interception respectively. The function G corresponds to a Poiseuille velocity profile and is independent of the particle's angular position.

$$G(\alpha, R_d/R_p) = \frac{8 \sin(\alpha f_1(\alpha, R/R_o)}{(R/R_o) f_o(\alpha, R/R_o)} \tag{2.22}$$

where

$$f_o = \pi \left[1 - \frac{1}{4}\left(\frac{R}{R_o}\right)^2\right] - \frac{4}{3}\left(\frac{15}{16}\pi - 2\right)\left(\frac{R}{R_o}\right)^2 \cos^2\alpha \tag{2.23}$$

and

$$
\begin{aligned}
f_1 = 1 &- \frac{1}{3}\left(\frac{R}{R_o}\right)^2 + \left(\pi - \frac{11}{3}\right)\cos^2\alpha - \frac{1}{3}\left(\frac{R}{R_o}\right)^2 \sin\alpha \\
&+ \left(\frac{2}{3} - \frac{\pi}{8}\right)\left(\frac{R}{R_o}\right)^4 \cos^2\alpha + \frac{1}{5}\left(\frac{R}{R_o}\right)^4 \sin^4\alpha \\
&+ \left(6 - \frac{15\pi}{8}\right)\left(\frac{R}{R_o}\right)^4 \cos^4\alpha + \left(\frac{7}{15} - \frac{\pi}{8}\right)\left(\frac{R}{R_o}\right)^4 \sin^2\alpha\cos^2\alpha
\end{aligned} \tag{2.24}
$$

The Stokes number term depends on the orientation of the ellipsoid particle and for each case it is given as

$$
St_{f_1} = \frac{C\rho d_f^2 \mu_o}{36\mu R_o} \tag{2.25}
$$

and

$$
St_{f_3} = \frac{C\rho d_f^2 \beta \mu_o}{36\mu\left[\left(1 - \frac{\pi^2}{16}\right) d_{f\parallel} + \frac{\pi^2}{16} d_{f\perp}\right]} \tag{2.26}
$$

Oseen (1927) has shown that $d_{f\parallel}$ and $d_{f\perp}$ are equal to the sedimentation shape factors defined earlier as Equation 2.17 and 2.16 respectively. The above equations allow for both the impaction and interception deposition efficiency to be calculated for both a case where the particle is aligned and randomly oriented with respect to the bifurcation.

Yu et al. (1986) also provided equations to calculate the deposition efficiency of an ellipsoid particle due to impaction at small Stokes number. Their model is based on an already established equation for impaction deposition of spheres given by Chan and Yu (1982) and shown below

$$
\eta_i = 0.768\theta St \tag{2.27}
$$

θ is the branch angle in radians and the 0.768 term is based on a bend to pipe radius ratio is equal to 8. In the geometry used in the study the actual bend to pipe radius ratio was equal to 3.21. For this value of bend to pipe radius ratio Equation 2.27 becomes

$$\eta_i = 0.989\theta St \tag{2.28}$$

It should be noted that the equation given by Chan and Yu (1982) is based on simple bend geometry and rotational velocity flow profile. The Stokes number in this case is defined as

$$St = \frac{\rho_o d_{ei}^2 U}{36\mu R} \tag{2.29}$$

ρ_o is equal is a given density equal to 1000 kg/m^3; d_{ei} is an equivalent diameter for impaction and is dependent on the orientation of the fiber. For an ellipsoid particle with its major axis perpendicular to the flow the equivalent diameter is given by Yu et al. (1986) as

$$d_{ei} = d_f \frac{3}{4} \left[\frac{\rho_o}{\rho} \left(ln(2\beta) + \frac{1}{2} \right) \right]^{1/2} \tag{2.30}$$

These equations give an alternate way to calculate the deposition due to impaction of both the aligned and magnetically aligned case of an ellipsoid particle.

Chapter 3

Method and Theory

3.1 Governing Equations

This section introduces the governing equations and the numerical scheme of the fictitious domain algorithm used in the study. The air traveling through the bifurcation was assumed to be a Newtonian and incompressible fluid so that the momentum and continuity equations can be described by Equation 3.1 and Equation 3.2 respectively.

$$\frac{\partial \mathbf{u}}{\partial t} + \mathbf{u} \cdot \nabla \mathbf{u} = -\nabla p + \frac{1}{Re} \nabla^2 \mathbf{u} \tag{3.1}$$

$$\nabla \cdot \mathbf{u} = 0 \tag{3.2}$$

where $\mathbf{u}$ and p are the fluid velocity and fluid pressure respectively. The Reynolds number Re is made up of a characteristic length, velocity and viscosity used to scale all other parameters. The equations governing the motion of the rigid particle are given below

$$\frac{d\mathbf{U}}{dt} = \frac{\rho_r - 1}{\rho_r}\frac{1}{Fr}\mathbf{e}_g + \frac{1}{\rho_r V}\mathbf{F} \tag{3.3}$$

$$\frac{d\left(\mathbf{I}\boldsymbol{\omega}\right)}{dt} \tag{3.4}$$

where $\mathbf{U}$, V, $\mathbf{I}$, and $\boldsymbol{\omega}$ represent the particle's velocity, volume, inertia tensor, and angular position respectively. The variable ρ_r is the ratio of the particle density over of the fluid density. The effect of gravity is included with the unit vector in the direction of gravity, $\mathbf{e}_g$, and the Froude number, Fr. The hydrodynamic force and torque acting on the particle is defined as

$$\mathbf{F} = \int_{\partial\Omega_p} \boldsymbol{\sigma} \cdot \mathbf{n} ds \tag{3.5}$$

$$\mathbf{T} = \int_{\partial\Omega_p} (\mathbf{x} - \mathbf{X}) \times (\boldsymbol{\sigma} \cdot \mathbf{n}) ds \tag{3.6}$$

$$\boldsymbol{\sigma} = -p\boldsymbol{\delta} + \frac{\nabla\mathbf{u} + (\nabla\mathbf{u})^T}{Re} \tag{3.7}$$

$\mathbf{X}$, $\boldsymbol{\sigma}$, $\boldsymbol{\delta}$, and $\mathbf{n}$ are the particle's center of mass position, stress tensor, Kronecker tensor, and unit outward normal to the particle boundary respectively. On the particle's boundary, a no-slip boundary condition is given as

$$\mathbf{u} = \mathbf{U} + \boldsymbol{\omega} \times (\mathbf{x} - \mathbf{X}) \tag{3.8}$$

3.1.1 Fictitious Domain Method

The algorithm used to solve both the fluid flow and particle trajectory is based on a fictitious domain method (FDM). The finite element algorithm was introduced by Diaz-Goano et al. (2003) as an improved method to that developed by Glowinski et al. (1999). Diaz-Goano et al. (2003) use the algorithm to study the sedimentation of a rigid spherical particle through a three dimensional incompressible fluid. The Lagrange multipliers for imposing the rigid body motion of the particle was removed and a more efficient version of the fictitious domain algorithm was introduced by Veeramani et al. (2007). This fictitious domain algorithm extends the fluid equations over the whole domain, including the particle domain, allowing for the use of a fixed Eulerian grid. A two-grid discretization component was added to the FDM algorithm by Dechaume et al. (2010) in order to handle the large difference in scales between the particle and bifurcation. The large-scale or macro grid discretizes the three dimensional bifurcation model. The high aspect ratio particle and fluid flow around it is discretized by a small-scale or micro grid. The macro grid is used to solve for the fluid flow in the absence of the particle. Due to the particle size and particle concentrations (Finlay, 2001) typical of drug delivery it is valid to assume the particle only affects the flow near its vicinity. Thus the resulting macro grid flow field is interpolated on the external boundary of the micro grid and the fluid and particle coupled equations are only solved over the micro grid. The incompressible Navier-Stokes equations are approximated by a second-order pressure-correction algorithm (Dechaume et al., 2010), combined with the method of characteristics for the advection operator. The resulting split

formulation is discretized in space by means of P2-P1 finite elements. A preconditioned conjugate gradient solver is used to solve the resulting linear system of equations. The discretization of the coupled equations in time is completed over three different sub steps. The first sub step is the advection-diffusion sub step. The position and orientation of the particle is predicted explicitly during this step using the following equation.

$$\boldsymbol{X}_i^{p,n+1} = \boldsymbol{X}_i^{n-1} + 2\delta t \boldsymbol{U}_i^n \tag{3.9}$$

δt in the above equation is the time step. Then $\boldsymbol{u}_1^1$ is solved over the entire domain using the following equations

$$\tau_0 \boldsymbol{u}_1^* - \frac{1}{Re}\Delta^2 \boldsymbol{u}_1^* = -\tau_1 \tilde{\boldsymbol{u}}_1^n - \tau_2 \tilde{\boldsymbol{u}}_1^{n-1} - \Delta p_1^n + \frac{\rho_{2,i} - \rho_i}{\rho_1}\boldsymbol{G} \text{ in } \Omega \tag{3.10}$$

$$\boldsymbol{u}_1^* = 0 \text{ on } \delta\Omega \tag{3.11}$$

where $\tau_0 = 3/(2d\delta)$, $\tau_1 = -2/(d\delta)$ and $\tau_2 = 1/(2d\delta)$. The velocities from time levels n and $n-1$ are represented by $\tilde{\boldsymbol{u}}_1^n$ and $\tilde{\boldsymbol{u}}_1^{n-1}$. The incompressibility constraint is applied during the following projection sub step. The following equations are used to apply this constraint.

$$\tau_0(\boldsymbol{u}_1^{**} - \boldsymbol{u}_1^*) = -\Delta(p_1^{n+1} - p_1^n) \text{ in } \Omega \tag{3.12}$$

$$\Delta \cdot \boldsymbol{u}_1^{**} = 0 \text{ in } \Omega \tag{3.13}$$

$$\boldsymbol{u}_1^{**} \cdot \boldsymbol{n} = 0 \text{ on } \delta\Omega \tag{3.14}$$

For the detailed procedure and equations used to solve the advection-diffusion and projection sub steps are given by Veeramani et al. (2007). The final sub step is the rigid body constraint applied to the micro grid boundary. The procedure to to apply the rigid body constraint and solve for the particle position has been given in detail by Roshchenko et al. (2011b).

3.2 Geometry Generation

A model was generated using the method described by Hegedűs et al. (2004) to create a morphologically realistic bifurcation using a computer aided design (CAD) program. The symmetric single bifurcation model used in this study is representative of a single airway found in generation 14-15. Figure 3.1 shows the three dimensional model. The dimensional parameters describing the single bifurcation model can be found in Table 3.1. The lengths and diameters were taken from Finlay et al. (2000). The radius of curvature, carina radius and bifurcation angle were taken from Horsefield et al. (1971).

Table 3.1: Summary of single bifurcation dimensions in millimeters

D_p	$L_p^{'}$	D_d	$L_d^{'}$	R^*	R_c	ϕ
0.61	0.62	0.49	0.92	0.98	0.049	50^o

3.3 Bifurcation Mesh Generation

Once the bifurcation model geometry is created in the CAD program (Pro/ ENGINEER) it was exported into the three dimensional finite element mesh generator program, Gmsh. For a in depth summary of the algorithms utilized and the program's capabilities the reader can refer to Geuzaine and Remacle

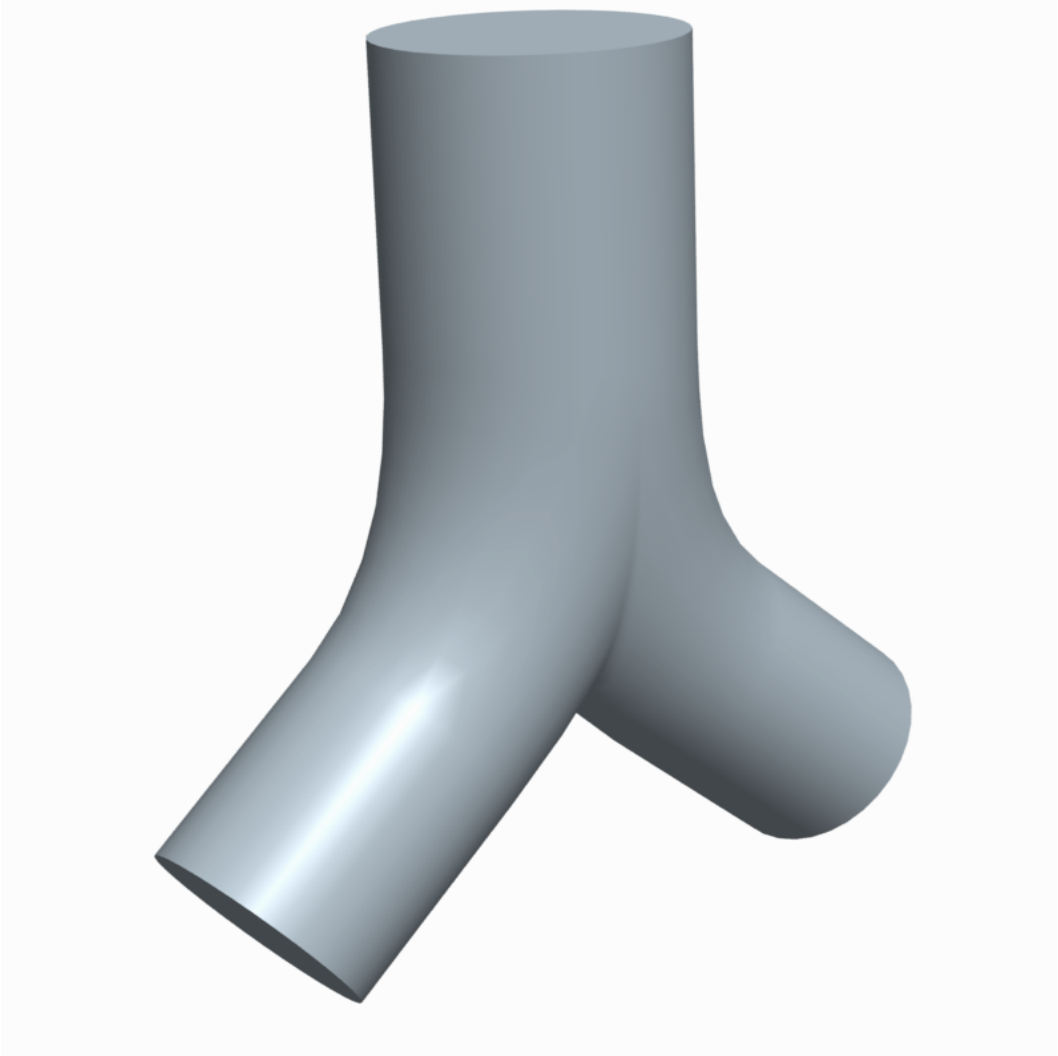

Figure 3.1: Single Bifurcation Geometry

(2009). The program was chosen due to its ability to quickly create a finite element grid compatible with the FDM algorithm. The disadvantage of this program is its limited ways to control mesh size in specific areas of the model. Grid spacing can be explicitly assigned to a geometry point but this is only applicable to geometry created within Gmsh. Instead grid spacing was based on a given minimum length, maximum length and the curvature of the boundaries. Due to the curvature of the boundary near the carina Gmsh

produces a smaller grid spacing in this area. With these options the 2-D surface grid was created using a combination of a "MeshAdapt" algorithm (Geuzaine and Remacle, 2009) and a 2-D Delaunay algorithm (Frey and George, 2000). Gmsh also allows for the grid spacing to be extended from the boundaries, which means the grid spacing within the bifurcation is calculated based on the nearest boundary. This constrained Gmsh to use the smallest grid spacing near the boundary and the carina. The 3-D grid was created using a Delaunay algorithm.

3.4 Steady Air Flow Analysis

3.4.1 Simulation Conditions

This section outlines the procedure used to simulate the steady air flow through a morphologically realistic single bifurcation using the FDM algorithm. Steady state fluid-only simulations were completed over five successively refined macro grids of the bifurcation model. The macro grid dimensions and flow parameters were rescaled to dimensionless values using a characteristic velocity, length and viscosity of 174.99 mm/s, 0.73 mm and 15.08 mm^2/s respectively. These characteristic parameters result in a Reynolds and Froude number of 8.47 and 4.28 respectively. Simulations were started with the velocity everywhere being zero except for the inlet. The time step used by the FDM method is given as a non-dimensional time step since all values have been rescaled by the characteristic velocity, length and viscosity. A non-dimensional time step of 1e-4 was used in order to ensure stability of the time integration over the whole domain. Once the maximum velocity residuals reached values less than 1e-7 the steady state simulation was considered

converged. The equations describing the different boundary conditions placed on the the bifurcation model are given below.

3.4.2 Inlet Boundary Conditions

A Poiseuille velocity profile, Equation 3.15, was prescribed at the inlet. A U_{max} of 125.0 m/s was prescribed, corresponding to a trachea flow rate of 18 l/min when assuming symmetrically branching airways. This is also considered to be a flow rate typical of tidal breathing flow. The validity of the inlet velocity profile was explored by also simulating the flow when an upstream bifurcation was added (see Appendix A). Poiseuille flow was determined to be a good representation of the inlet velocity profile (see Appendix A), given by

$$V = U_{max}(1 - \frac{r^2}{R_p^2}) \tag{3.15}$$

3.4.3 Outlet Boundary Conditions

Equation 3.16 and Equation 3.17 describe the condition placed on the velocity and pressure at the outlet respectively.

$$\frac{\partial \mathbf{u}}{\partial \mathbf{n}} = 0 \tag{3.16}$$

$$p_{outlet} = 0 \tag{3.17}$$

3.4.4 Bifurcation Wall Boundary Condition

The wall boundary of the bifurcation was given a no slip condition. Equation 3.18 represents this boundary condition.

$$w_{wall} = v_{wall} = u_{wall} = 0 \tag{3.18}$$

3.4.5 Flow Pattern Analysis

The fluid flow within the bifurcation was completed on five different refined grids in order to ensure sufficient grid refinement. A grid convergence index (GCI) value was calculated between grids using the expression given by Celik et al. (2008),

$$GCI = F_s \frac{\varepsilon_{rms}}{r^p - 1} \tag{3.19}$$

where ε_{rms}, p, r and F_s are the root-mean-square (RMS) error, order of method, refinement factor, and factor of safety respectively. The refinement factor is the ratio of the number of nodes between the refined and coarse grid. When proper grid halving (r=2) is not possible the GCI value can be used to estimate the RMS error (Celik et al., 2008). A value of 3 was used for the safety factor to account for the refinement fact r always being less than 2. The ε_{rms} value was calculated from the velocity relative error between 1000 points inside the bifurcation. A second-order procedure is used in the discretization method so a value of 2 was used for p (Guermond et al., 2006).

3.5 Particle Trajectory Simulations

3.5.1 Particle Geometry

The high aspect ratio particle geometry was represented by an ellipsoid described by the equation below.

$$\frac{x^2}{a^2} + \frac{y^2}{b^2} + \frac{z^2}{c^2} = 1 \tag{3.20}$$

Where a, b are the equatorial radii and c is the polar radius of the ellipsoid. The aspect ratio in this case is the ratio between the equatorial and polar diameter. The equatorial diameter and aspect ratio in this study were 0.5 μm and 6 respectively. Particle dimensions were based on the VMD and VML used in the *in vitro* study done by Martin and Finlay (2008b).

3.5.2 Micro Grid Geometry and Mesh Generation

The micro grid is made up of three different shapes in order to control the grid sizing throughout the grid. Figure 3.2 shows a schematic of the micro grid consisting of an outer rectangular box, middle cylinder and an inner ellipsoid. The geometry was created using the geometry creation feature of Gmsh. To create the 2-D surface grid was created using a combination of a "MeshAdapt" algorithm (Geuzaine and Remacle, 2009) and a 2-D Delaunay algorithm (Frey and George, 2000). Second order unstructured tetrahedral elements were used to fill the micro grid domain. Grid spacing sized was controlled by the characteristic length prescribed to the points making up the different micro grid shape surfaces.

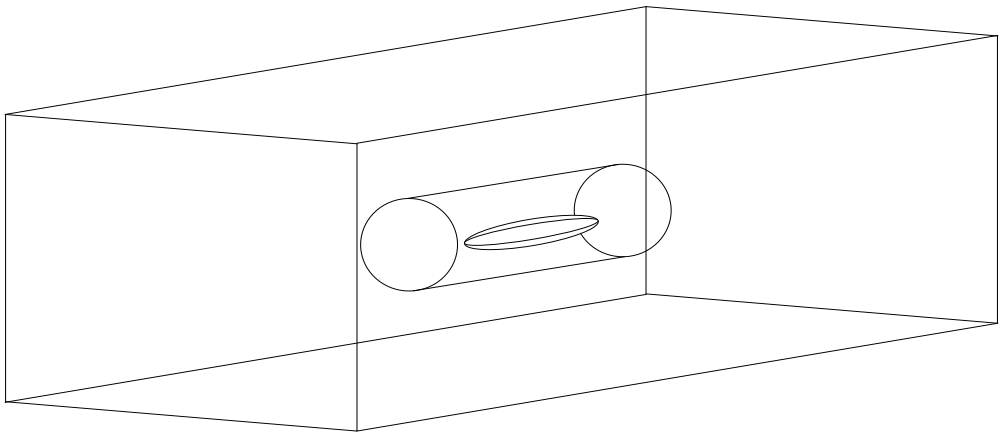

Figure 3.2: Schematic of micro grid geometry consisting of three separate control shapes. Different grid spacing was used within the rectangular box, cylinder and ellipsoid.

3.5.3 Effect of Particle Time Step

For the particle trajectory simulations, a non-dimensionalized particle time step is given explicitly. To study the effect of the time step on the particle trajectory, several simulations were done at different time step values. This was done for a particle which was allowed to naturally (i.e. free to rotate) travel through the bifurcation. The particle translational and angular position was compared between the simulations to find an acceptable time step to utilize in the deposition simulations.

3.5.4 Effect of Micro Grid Size and Spacing

Another source of error is the micro grid where the fluid flow nearest to the particle and particle forces are calculated. Particles were allowed to deposit on the walls in simulations done with different degrees of refinement. The change in particle trajectory due between these different simulations due to

mesh refinement was calculated. Also studied was the effect of changing the size of the rectangular box. With the results of this component of the study, a suitable micro grid mesh could be chosen for the deposition study in Section 3.6.

3.5.5 Effect of Solver Convergence Criterion

The effect of changing the conjugate gradient solver convergence criterion on the particle trajectory was also studied. The difference in particle trajectory was recorded with the convergence criterion set to 1e-4, 1e-7 and 1e-9. The final solver convergence criteria value was chosen based on the change in final deposition point of the particle.

3.5.6 Computational Equipment and Simulation Run Time

All simulations were completed on Dell PowerEdge 2900 servers with two Intel E5430 processors and 16 Gb of memory. A single server is capable of running eight separate threads. A single particle simulation on four threads resulted in a computational time per time step between 5 and 30 seconds. For a single particle simulation with a non-dimensional time step of 1e-3 the simulation would be completed with 1-2 weeks depending on the inlet position of the particle.

3.6 Deposition Simulations

3.6.1 Deposition Efficiency Calculation

The deposition efficiency was defined as the ratio between the flow rate through a deposition area at the inlet and the total flow rate at the inlet

of the bifurcation. This deposition efficiency is expressed below

$$Q = Q_{deparea}/Q_{inlet} \tag{3.21}$$

The definition of deposition used for this study is restricted to monodispersed particles with a constant particle concentration density across the inlet. Thus the number of particles entering a given location at the inlet is only affected by the velocity profile of the inlet. The deposition area boundary is made up of the initial inlet positions of particles which successfully deposited in the single bifurcation. Since the initial positions of particles were isolated to only one quarter of the inlet geometry there is an assumption made that the deposition area is both continuous and symmetric across the two planes of the bifurcation. The boundary of the area is made up of straight lines between each data point. Thus between each injection point there is straight line represented by the following equation.

$$X_i(z) = mz + b \tag{3.22}$$

Figure 3.3 shows a schematic of the deposition area made up of the particle initial starting points and curve fitted lines.

The flow rate through the deposition area was calculated knowing the boundary of the area and the velocity profile at the inlet. The deposition flow rate was defined as the following equation

$$Q_{deparea} = \int\int V(x,z)dxdy \tag{3.23}$$

The velocity profile expressed earlier as Equation 3.15 can be expressed in

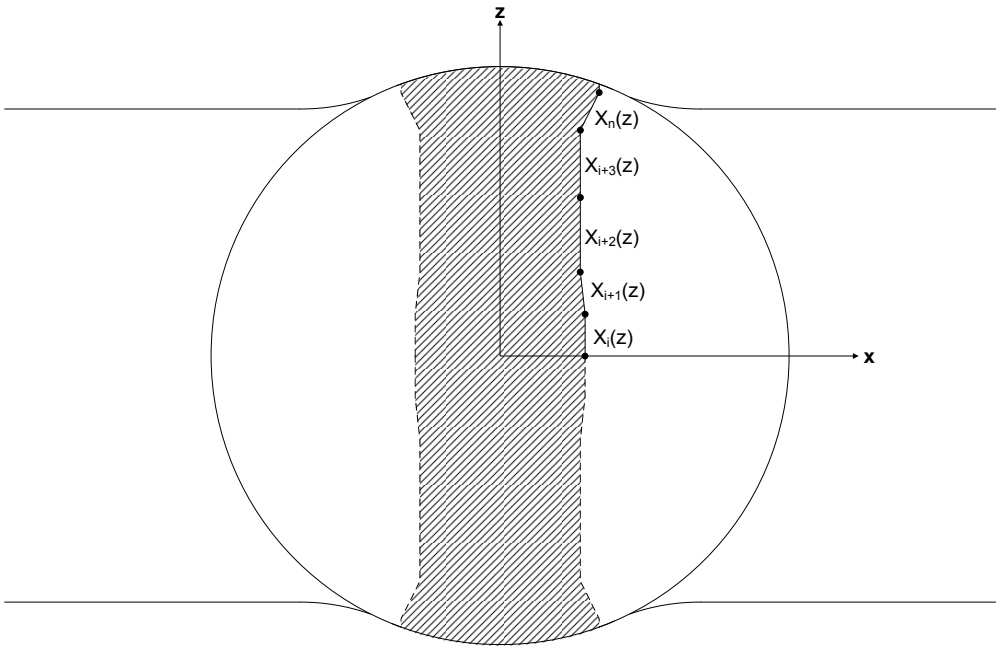

Figure 3.3: Schematic of how the "deposition" area is defined

Cartesian coordinates and the deposition flow rate can be defined as Equation 3.24. Once the deposition inlet points (i.e. X_i) are known, Equation 3.24 can be calculated to find the flow rate through the deposition boundary. This method of calculating deposition follows the idea of a limiting trajectory boundary that has been used previously in other studies to calculate deposition (Cai and Yu, 1988; Asgharian and Yu, 1989).

$$Q_{deparea} = \int_0^{Z_o} \int_0^{X_i(z)} \left\{ V_{max} \left(1 - \frac{x^2 + z^2}{R_p^2} \right) \right\} dxdz \qquad (3.24)$$

For the magnetically aligned case there is deposition along the outside of the bifurcation wall that also must be accounted for. Once the particle's major axis is aligned with the x-axis, the particle may now deposit on the bifurcation wall. Particles within half a particle length in the x direction are

considered to be deposited and an outside deposition area can be defined. An outside deposition efficiency was calculated by finding the flow rate through the outside deposition area. This was not completed for the aligned case since the flow rate within a particle radius of the outside wall is negligible.

3.6.2 Deposition Efficiency: Strong Streamline Alignment Case

In order to measure the enhancement in deposition due to the particle alignment a base case to compare deposition is needed. Typically the base case deposition efficiency would be calculated by allowing the particle to deposit with an unconstrained angular position. However, during the time step sensitivity analysis (see Section 4.2) it was found that for the particle's angular velocity to be simulated accurately a minimum time step of 1e-4 is needed. The small time step in combination with the trial and error nature of calculating the deposition made it unfeasible to calculate the deposition efficiency. The solution was to initially prescribe the particle's angular position to be constant and parallel to the inlet streamlines. The angular position was then changed again to align with the streamlines once the particle entered the daughter bifurcation. This would in effect estimate the path of a particle with strong tendency to align with the streamlines. With an aspect ratio of either 6 or 20 (the aspect ratio considered here), the rotational Peclet number Pe, which is the ratio of the hydrodynamic rotation and the Brownian rotation, is much greater than 1, so that induced rotation is negligible. Also, the current flow conditions result in an average period of rotation (Jeffery, 1922; KR, 1928) equal to 7 and 17 times greater than the average particle residence time for a particle with an aspect ratio of 6 and 20, respectively. Therefore, although the above procedure is not ideal, it is a reasonable approximation for the

naturally occurring or unconstrained case. The particle was injected to the inlet with a translational velocity identical to the surrounding fluid and a non-dimensional time step of 1e-3 was used.

3.6.3 Deposition Efficiency: Magnetically Aligned Case

To estimate the deposition of the magnetically aligned particles the angular position of the particles was again constrained. This major axis of the particle was constrained so that it was parallel to the inlet boundary but perpendicular to the inlet flow. This is the type of alignment that occurred in the study done by Martin and Finlay (2008b). The initial translational velocity of the particle was prescribed to match the surrounding fluid. A non-dimensional time step of 1e-3 was used.

3.7 Theoretical Deposition Calculations

Theoretical deposition models were used to calculate the deposition probability in order to both gain an understanding of the effect of changing certain parameters and to be able to compare analytical model estimates to the results using the FDM algorithm. The deposition due to impaction and interception was calculated using the theory given by Cai and Yu (1988) and Yu et al. (1986) for fibers in a bifurcating airway and under parabolic flow conditions. The sedimentation deposition probability was calculated using the model given by Heyder and Gebhart (1977) in combination with the settling velocities for a fiber expressed by Harris and Fraser (1976). The deposition probability for each deposition mechanism was calculated separately and summed to find the total deposition. The particle geometry

used was an ellipsoid particle with a diameter of 0.5 μ m and a density of 1190 kg/m^3. The deposition probability was calculated for an aspect ratio of 6 and 20. The deposition probability due to sedimentation, impaction, and interception was calculated for both a particle aligned with the flow and a particle aligned perpendicular to the inlet flow. Finally these calculations were done using the flow conditions and geometry used in this current study.

Chapter 4

Results

4.1 Steady Flow Field

The flow pattern through the bifurcation model is shown in Figure 4.1. The Poiseuille velocity profile from the parent inlet continues until the transition region where the flow diverges symmetrically into the daughter airways. The axial velocity profile along the line D-D' is seen in Figure 4.2. Although the velocity profile is parabolic, the point of maximum velocity is located slightly towards the outer side of the bifurcation. The axial velocity profile regains a Poiseuille shape in the straight portion of the daughter tube.

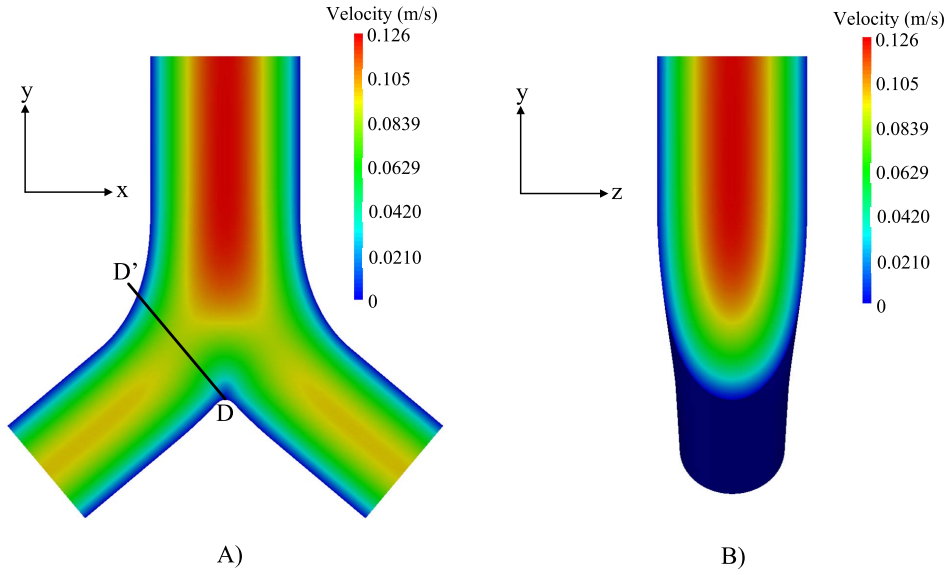

Figure 4.1: Air velocity profile of inspiratory flow through the small bifurcation model. Velocity profiles are from cuts at the center of the bifurcation in two different planes A) y-x plane B) y-z plane

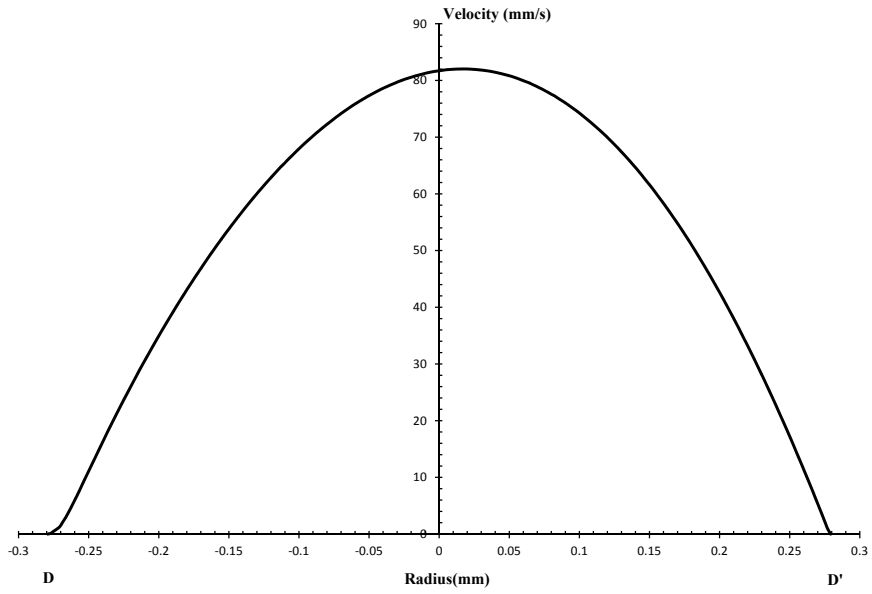

Figure 4.2: Axial velocity profile along the line D-D$'$ seen in Figure 4.1

The velocity profile at a distance 0.146 mm downstream of the transition region was compared with different lengths $L_d^{'}$. Changing the $L_d^{'}$ length from 0.0461 mm to 1.846 mm changed the three-dimensional velocity profile by less than 0.01%, indicating that our outlet boundary placement does not affect the simulation results.

The values associated with the GCI analysis are shown in Table 4.1. With each grid refinement the GCI value decreased, resulting in a 1.39% GCI value for the most refined grid. The most refined grid was used for all the particle trajectory simulations. A fifth grid (with 894 x 10^3 elements) was created to compare to the most refined grid. The available computation resources did

not allow for a grid with a sufficient refinement with respect to the grid with 1314 x 10^3 elements to be created.

Table 4.1: Results of grid convergence index (GCI) analysis completed on the macro grid representing the steady flow through the small bifurcation model. Here, r is the refinement factor, ϵ_{rms} is the rms error and the GCI is the grid convergence index (Celik et al., 2008)

Number of elements (10^3)	**r**	ϵ_{rms}	**GCI (%)**
168-386	1.32	1.77	7.14
386-1314	1.50	2.15	5.12
894-1635	1.22	0.23	1.39

4.2 Particle Simulation Sensitivity Analysis

Table 4.2 shows the relationship between the dimensionless time step used and the point of maximum and minimum angular velocity. These results are also compared to the theoretical given by maximum and minimum angular velocity Jeffery (1922). As the dimensionless time step decreased from 1e-3 to 5e-5 the results approached the theoretical results. In terms of the particle trajectory, the dimensionless time step had a negligible effect, as will be discussed in Chapter 5.

Table 4.2: Change in angular position of the maximum and minimum angular velocity of the particle occurring with different dimensionless time steps

Time Step	**Max. $\dot{\theta}$**		**Min. $\dot{\theta}$**		**θ at Max. $\dot{\theta}$**		**θ at Min. $\dot{\theta}$**	
(10^{-3})	**Result**	**Δ Theory**	**Result**	**Δ Theory**	**Result**	**Δ Theory**	**Result**	**Δ Theory**
Theory*	3.03	-	0.08	-	180.0^o	-	90.0^o	-
1.0	2.15	0.89	0.80	-0.72	213.4^o	-33.4	119.2^o	-29.2
0.5	2.47	0.56	0.28	-0.20	205.8^o	-25.8	104.7^o	-14.7
0.25	2.77	0.27	0.09	-0.01	199.0^o	-19	90.9^o	-0.9
0.1	3.00	0.029	0.08	0	189.6^o	-9.6	90.2^o	-0.2
0.05	3.07	0.040	0.08	0	185.6^o	-5.6	89.6^o	0.4

*Theory results based on equations given by Jeffery (1922)

The change in deposition point was also recorded with each change in the micro grid. This was only done for a particle with a fixed angular position corresponding to the magnetically aligned case. Doubling the number of elements inside the micro grid resulted in a final position 0.019 mm further downstream. Doubling the size of the micro grid resulted in the particle depositing 0.05 mm farther downstream. Doubling the number of elements for a particle with an aspect ratio of 20 resulted in the particle depositing less than 0.001 mm downstream.

Changing the convergence criteria of the conjugate gradient solver from 1e-4 to 1e-7 resulted in the particle depositing 0.135 mm downstream. A smaller difference in final position of 0.005 mm downstream was seen when changing the convergence criteria from 1e-7 to 1e-9. Therefore a value of 1e-7

was used for the solver criterion.

4.3 Deposition Efficiency

The inlet deposition boundaries for a particle with an aspect ratio of 6 and 20 are shown in Figure 4.3 and Figure 4.4 respectively. The x and z-axis in both figures were normalized by the length of a particle with an aspect ratio of 6 and correspond to the axes shown previously in Figure 3.3. For brevity the unconstrained case and the magnetically aligned case will be defined as Case [1] and Case [2], respectively. Near the center of the inlet the deposition boundary for Case[1] and Case[2] are approximately the same. For both Case [1] and Case [2] the deposition boundary begins to decrease at a normalized z position of 10, with the Case [1] deposition boundary decreasing by a larger amount. At a normalized z position equal to 65 the deposition boundary for both Case [1] and Case [2] now begin to significantly curve. The Case [1] deposition increases above the Case [2] boundary at a z position of 74 before the Case [2] is larger again at a z position of 90.

For a particle with an aspect ratio of 20 the deposition boundaries have a relatively constant slope boundary shape for both Case [1] and Case [2] near the center. Both deposition boundaries begin to curve when nearing the outside bifurcation boundary at a normalized z position of 40. The Case [1] deposition boundary is never greater than the Case [2] deposition boundary.

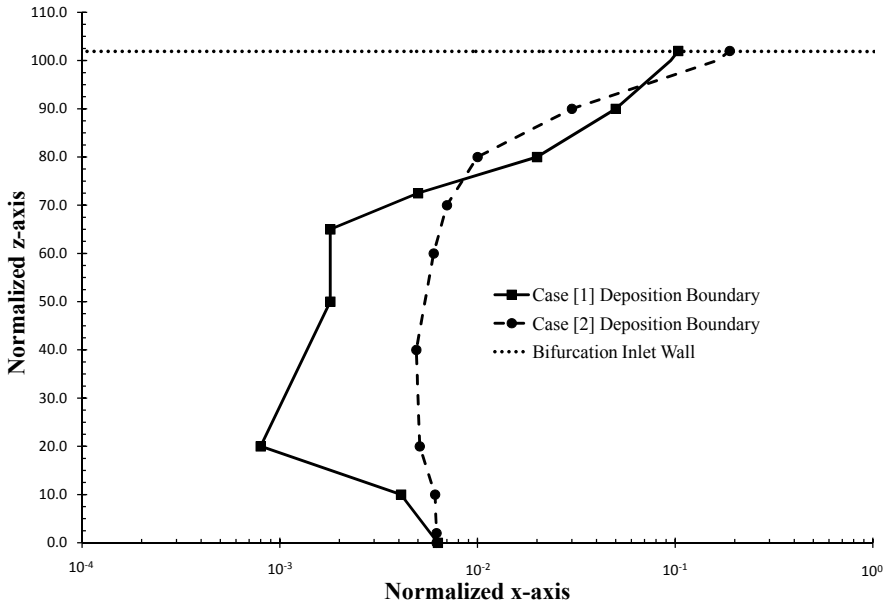

Figure 4.3: Case [1] and Case[2] isolated deposition regions at the bifurcation inlet for a particle with an aspect ratio of 6. Deposition boundary lines represent the division where the particles entering to the left deposit and those to the right do not deposit. The x and z position correspond to the axes located at the center of the inlet seen previously in Figure 3.3. The x and z position were normalized by dividing the dimensionless position by the length of a particle with an aspect ratio of 6. The bifurcation inlet wall is the outer limit boundary of the fluid domain at the inlet.

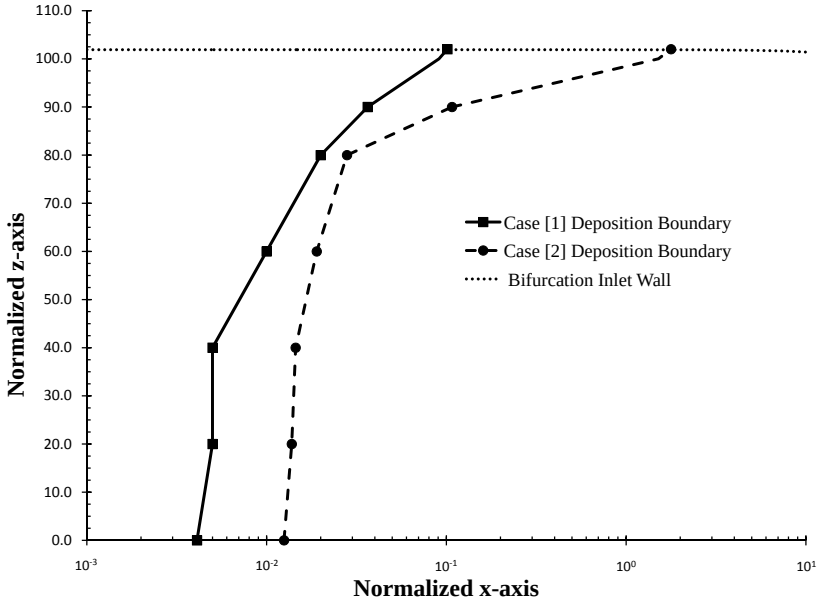

Figure 4.4: Case [1] and Case[2] isolated deposition regions at the bifurcation inlet for a particle with an aspect ratio of 20. Deposition boundary lines represent the division where the particles entering to the left deposit and those to the right do not deposit. The x and z position correspond to the axes located at the center of the inlet seen previously in Figure 3.3. The x and z position were normalized by dividing the dimensionless position by the length of a particle with an aspect ratio of 6. The bifurcation inlet wall is the outer limit boundary of the fluid domain at the inlet.

The measured deposition efficiency and deposition boundary error for an aspect ratio of 6 and 20 is given in Table 4.3. The deposition boundary error has been defined as the difference between the deposition efficiency given by the particles that deposited and the non-deposited particles. The deposition boundary error ranged between 0.00057% and 0.00118%. The deposition error was always less than 14% of the actual deposition efficiency.

The deposition efficiency due to outside interception deposition at the inlet for Case [2] was 0.0048% and 0.0540% for a particle with an aspect ratio of 6 and 20 respectively.

Table 4.3: Deposition efficiency results based on the inlet deposition boundary for each case and aspect ratio. The deposition boundary error is the difference between the deposition efficiency given by the deposition region of particles that deposited and the deposition boundary of particles that did not deposit.

	Aspect Ratio	**Deposition (%)**	**Deposition Boundary Error (%)**
Case [1]	6	0.0092	0.00118
	20	0.0149	0.00111
Case [2]	6	0.0131	0.00059
	20	0.0515	0.00057

The enhancement factor, defined as the ratio between the Case [1] and Case [2] deposition efficiency, is given in Table 4.4 for both an aspect ratio of 6 and 20. The amount of deposition enhancement increased by a factor of 2.4 when the particle aspect ratio was changed from 6 to 20 (an aspect ratio increase by a factor of 3.3). Also given in Table 4.4 is a deposition range which takes into account the deposition boundary error for each deposition efficiency measurement and represents the smallest and largest possible value for enhancement. If the outside interception at the inlet is included, the enhancement factors increase to a value of 1.95 and 7.09 for an aspect ratio

of 6 and 20 respectively.

Table 4.4: Deposition enhancement between Case [1] and Case [2] for both aspect ratio 6 and 20

Aspect Ratio	**Deposition Enhancement**	**Deposition Boundary Range**
6	1.43	1.27-1.49
20	3.46	3.22-3.50

4.4 Theoretical Deposition Results

The theoretical deposition due to impaction, interception, and sedimentation was calculated for each case. The portion of the deposition efficiency due to each deposition mechanism is given in Table 4.5. A range was given for the deposition efficiency due to impaction because two different theoretical equations were tested. The lower limit and upper limit was calculated using the theory given by Yu et al. (1986) and Cai and Yu (1988) respectively. It was also assumed that there would be no deposition due to interception in the unconstrained case. The deposition due to sedimentation and impaction was comparable to each other for both unconstrained and magnetically aligned case. The highest deposition efficiency was due to the interception in the magnetically aligned case. Interception deposition is approximately 2 and 6 times larger than the interception and sedimentation deposition combined for an aspect ratio of 6 and 20 respectively. An interesting result from Table 4.5 is that without interception, the deposition efficiency is larger for the unconstrained case than the magnetically aligned case. The deposition

due to impaction and sedimentation alone is approximately 10 to 20 percent more for the unconstrained case than the magnetically aligned case. The deposition enhancement when the unconstrained case and magnetically aligned case are compared was also calculated and is shown in Table 4.6. As expected, the theoretical deposition for aspect ratio of 20 is larger than for an aspect ratio of 6. The enhancement with aspect ratio of 20 is approximately 1.8 times that of the enhancement with an aspect ratio of 6.

Table 4.5: Theoretical deposition probabilities due to sedimentation, impaction and interception for each Case and aspect ratio combination. The lower and upper range for the impaction probability is due to two different methods used.

	Aspect Ratio = 6		Aspect Ratio = 20	
	Unconstrained Case (%)	Magnetically Aligned (%)	Unconstrained Case (%)	Magnetically Aligned (%)
P_{sed}	0.0351	0.0418	0.0510	0.0608
P_{imp}	0.0363 - 0.0565	0.0273 - 0.0415	0.0582 - 0.0887	0.0383 - 0.0582
P_{int}	N/A[c]	0.216	N/A[c]	0.720
P_{total}	0.0713 - 0.0916	0.2849 - 0.2992	0.1092 - 0.1397	0.8185 - 0.8384
Enhancement	3.27 - 3.99		6 - 7.49	

[a] Impaction probability calculated using the theory given by Yu et al. (1986)was used.

[b] Impaction probability calculated using the theory given by Cai and Yu (1988) was used.

[c] Interception does not apply since the particle is assumed to be aligned with the flow.

Table 4.6: Absolute and relative difference between the theoretical total deposition and the numerically calculated total deposition.

	Absolute Deposition Difference (%)		Relative Deposition Difference	
Aspect Ratio	Unconstrained	Magnetically Aligned	Unconstrained	Magnetically Aligned
6	0.0695 - 0.0898	0.2718 - 0.286	7.57 - 9.77	20.69 - 21.78
20	0.1101 - 0.1406	0.767 - 0.7869	7.39 - 9.44	14.88 - 15.27

Chapter 5

Discussion

5.1 Steady Flow Field

As expected, for a relatively low Reynolds number the flow pattern through the bifurcation was laminar and a Poiseuille like velocity profile occurred. The flow pattern through the transition area is no longer a symmetrical Poiseuille profile but the point of maximum velocity is skewed towards the outside of the bifurcation. This is the velocity profile near the inner wall of the bifurcation and thus affects deposition. If the mass flow of particles is concentrated near the inside wall (which is the case in higher Reynolds number flow), more particles have the opportunity to deposit. The importance of the flow pattern near the carina is discussed further when comparing our results to the theoretical results. To ensure that flow pattern through the bifurcation was not affected by the outlet boundary conditions the daughter length $L_d^{'}$ was increased by a factor of 4. With very little change in the flow pattern it can be concluded that the value of $L_d^{'}$ used in this study did not have any effect on the upstream flow. Longest and Vinchurkar (2007) studied the effect of the GCI value on an unstructured tetrahedral mesh

in a bifurcation. During their study they found that the GCI values could increase with refinement. They attributed this type of increase to round off error. In this study the GCI values decreased with refinement. Longest and Vinchurkar (2007) were also able to show that an unstructured tetrahedral mesh with a GCI value of about 5% was able to give reasonably accurate deposition results when compared to experiments.

5.2 Particle Simulation Sensitivity Analysis

An important result of the sensitivity analysis was the fact that a very small time step is needed to accurately simulate the angular movement of the particle as it travels through the bifurcation. The time step needed makes it unrealistic to do enough particle simulations to get an estimate for the deposition efficiency. The computational time would be increased from approximately a week to months. Therefore we would not be able to obtain our base case to compare to the case of the magnetically aligned particles. This resulted in having to instead force the angular position of the particle to align to the streamlines throughout the particle's trajectory. Ideally we would like to quantify the effect of changing the particle micro grid parameters by comparing the change in deposition efficiency results. The combination of long simulation time and the trial and error aspect of our method prevented this. However we can still gauge the significance of our sensitivity results by considering the relationship between the initial position and final position of the particle trajectory. For a fixed particle with an aspect ratio of 6 to deposit 0.05mm farther downstream, the inlet normalized x position would have to be increased by at most 0.0007. This change in the inlet position is less than

the typical distance between the deposition boundary and the non deposited boundary. Thus the deposition boundary error is the largest source of error in our analysis, which in the next section is shown not to significantly change our results. For both the aspect ratio of 6 and 20, changing the grid resolution did not greatly change the final deposition point of the particle. Increasing the solver convergence criteria from 1e-7 to 1e-4 had a significant effect on the particle trajectory. Since decreasing the convergence criteria from 1e-7 to 1e-9 had a negligible effect on particle trajectory the convergence criteria value of 1e-7 was prescribed for all the particle simulations used to estimate deposition efficiency.

5.3 Deposition Efficiency

The shape of the different deposition boundaries can be rationalized by considering the different deposition mechanisms involved. Since the velocity profile and geometry near the center (i.e. $x = z = 0$) does not change significantly, particles near this area encounter very similar flow conditions and geometry. This explains why near the center the deposition boundary is constant, while near the inlet wall the velocity profile and geometry is changing much more drastically. Also as one nears the wall, the conditions encourage deposition due to interception and sedimentation. The combination of interception and sedimentation also explains why the value of z where the deposition boundary begins to curve out in the x direction is different for each aspect ratio. A higher aspect ratio would increase the probability of deposition from sedimentation and impaction due to the particle's increased mass and length. Therefore it is reasonable for the position where the

boundary begins to curve outward is further from the wall for a particle with aspect ratio of 20 than for a particle with an aspect ratio of 6. The unconstrained case deposition boundary being greater than the magnetically aligned case boundary at a normalized z position of 74 can be explained by understanding that the interception deposition becomes less important than the sedimentation deposition. The orientation of the particle in the unconstrained case is more ideal for sedimentation; therefore an aspect ratio of 6 is not long enough to overcome the difference until much closer to the wall. It is near the wall where the magnetically aligned case deposition boundary is now extending past the unconstrained case deposition boundary. Since the bifurcation diameter decreases as one enters the transition region of the bifurcation, particles have a greater probability of depositing due to interception near the wall.

The calculated theoretical deposition seen in Table 4.5 is 7-20 times greater than our numerically measured deposition efficiency. The difference between measured and theoretical deposition is much greater in the magnetically aligned case than the unconstrained case. This is due to the theoretical interception deposition being larger than the sedimentation and impaction deposition efficiency combined. Although the theoretical interception calculation corresponds to a randomly oriented particle the difference in angular position does not account for the difference. Instead the discrepancy can be attributed to the difference in the theoretical and simulation velocity profile near the carina. The theoretical axial velocity profile near the carina (line D-D$'$ in 4.1) is a parabolic curve with a maximum velocity at the carina. The theoretical velocity profile concentrates the flow near the carina and consequently this would estimate higher deposition than a parabolic profile for impaction and

interception case. This discrepancy was not unexpected since for a fiber with a diameter between 1.2-2.3μm and an aspect ratio between 8.3-16.7, Cai and Yu (1988) over estimated the results found by Myojo (1990) by 2.2-27.8 times.

The model by Yu et al. (1986) has also shown that their model tends to over estimate experimental data. This is what the current results are also showing. Happel and Brenner (1965) used a low Reynolds approach to show for a spherical particle within 5 particle radii of a wall the settling velocity of the particle decreases. The particle residence time near the wall is large enough that the near wall effects can affect deposition due to sedimentation. For the magnetically aligned case, the alignment of the particle would actually cause the particle to translate away from the wall once it enters the daughter tube. This is because the alignment of the particle is no longer perpendicular to the flow but instead at an angle that results in a hydrodynamic force normal to the wall and thus a decrease in settling velocity. Therefore it is also not unexpected that the computational results would underestimate deposition relative to the theoretical sedimentation result.

Although it was assumed each deposition mechanism is occurring independently, several common theories were used to combine the theoretical results but there was no significant changes in the results(Asgharian and Anjilvel, 1994; Balásházy et al., 1990).

The absolute deposition efficiencies given by the *in vitro* Martin and Finlay (2008b) were much greater than what was found using the FDM algorithm. Although the geometries are similar, there are differences in both the geometry and particle properties that account for this discrepancy between results. It is a combination of the Brownian motion and geometry

that accounts for the largest difference. In order to manufacture the *in vitro* models, both the parent and daughter lengths in Martin and Finlay (2008b) were made much longer that was anatomically correct. For instance the parent and daughter lengths are 10 and 5 times longer in the *in vitro* model than in the computation model. Using the theory given by Asgharian and Ahmadi (1998) we can estimate the amount of deposition due to Brownian motion. For a particle with a diameter of 0.5 μm and an aspect ratio of 6, the deposition due to Brownian motion in the parent and daughter portion of our computational bifurcation is estimated to be 0.03% and 0. 068% respectively. However, for the *in vitro* model geometry and the same particle parameters the deposition in the parent and daughter are 0.239% and 0.155% respectively. Comparing the deposition between the *in vitro* and computational model we see that the Brownian motion was more important in the *in vitro* model due to the longer length parent and daughter lengths.The difference due to Brownian motion between the *in vitro* and computational model is increased due to a polydispersed aerosol being used in the *in vitro* experiments. Thus there would be an increase in deposition due to particles with much smaller diameters than 0.5m. It is known that when optimizing delivery a monodispersed aerosol with a diameter in the range of optimal size (Balásházy et al., 2007) should be used and thus it is expected that future experimental iterations of this method would use monodispersed aerosol that would not include or at least limit the smaller sized particles.

Considering these differences the deposition enhancement factor of 1.7 seen in the *in vitro* study is still in reasonable agreement with the computational enhancement factor of 1.43 and 1.95 if the outside interception is included.

5.4 Deposition Enhancement

Increasing the aspect ratio of the particle, the deposition efficiency of the unconstrained case would also increase. In this study the deposition increased by a factor of 1.62 when the aspect ratio increased from 6 to 20. By magnetically aligning the particle, the effect of changing the particle aspect ratio was larger, as the deposition increased by a factor of 3.92, suggesting that the magnetic alignment method takes better advantage of increasing particle lengths. This is important in terms of therapeutic effects since the mass deposited also increases with increased particle length. The deposition enhancement when applying the magnetic alignment method did not increase in direct equality with the increase in aspect ratio. Instead, for a particle aspect ratio change from 6 to 20 (a factor of 3.33) the deposition enhancement increased by a factor of 2.42. This suggests that with the use of longer fibers the magnetic method could be over 2 times more effective than what was previously seen in the study done by Martin and Finlay (2008b). By using aerosols where the VML and VMD produce an aspect ratio of at least 20 the local deposition could be increased by a factor of 3.46. The magnetic alignment could significantly improve drug delivery efficacy and in turn improve therapeutic effects as such that aggressive drugs can be used within their dose limiting toxicity.

Chapter 6

Conclusion

In this study a fictitious domain algorithm was successfully used to simulate the deposition of high aspect ratio particles through a morphologically realistic bifurcation. The bifurcation flow conditions and geometry were based on accepted values for typical tidal breathing through a generation 14-15 lung bifurcation. A thorough numerical sensitivity analysis was completed for all the numerical parameters involved in both the steady flow field and particle trajectory simulations. An important conclusion from this study was that for a particle with unconstrained angular position, the minimum non-dimensional time step needed was 1e-4. Even with state of the art computational equipment this resulted in particle trajectory simulations times of up to a month. The computation time is the largest disadvantage to the FDM algorithm and is a large obstacle if it is used for further deposition simulations. In this study the author suggested a different approach to estimating the deposition of a unconstrained particle. The particle's angular was constrained so that it remained aligned with the flow streamlines, an assumption verified in this study. This allowed for a smaller time step to be used to calculate the unconstrained case deposition efficiency.

By simulating both the unconstrained and magnetically aligned case, the deposition efficiency for each case could be estimated for an ellipsoid particle with a diameter equal to 0.5 μ. Due to the computational resources needed for a single simulation the deposition efficiency had to be calculated using a method adapted from previously used limiting trajectory methods. This resulted in a deposition area at the inlet for each case and aspect ratio size. These deposition boundaries gave insight on the importance of different deposition mechanisms (interception, sedimentation and interception) for the different bifurcation regions, particle sizes and also between the unconstrained and magnetically aligned case. The deposition efficiencies were verified by comparing to well known theoretical deposition equations.

Finally it was found that increasing the aspect ratio of the particle from 6 to 20 could result in over 2 times more local enhancement. These results show that the effectiveness of the magnetic alignment method can be increased using aerosol particles with higher aspect ratios. High aspect ratio particles have been shown to be capable of penetrating to the distal components of the lung but with larger dosage when compared to their spherical counterpart. Using the magnetic targeting method deposition, could be increased by 3.4 times in targeted locations of the lung and in the case of aggressive medicine less damage would be done to healthy parts. This study has further shown the great potential of the magnetic alignment with respect to pharmaceutical aerosols (e.g. chemotherapeutic agents) to treat lung disease.

Bibliography

Asgharian, B. and Ahmadi, G. (1998). Effect of Fiber Geometry on Deposition in Small Airways of the Lung. *Aerosol Science and Technology*, 29(6):459–474.

Asgharian, B. and Anjilvel, S. (1994). A Monte Carlo calculation of the deposition efficiency of inhaled particles in lower airways. *Journal of Aerosol Science*, 25(4):711–721.

Asgharian, B. and Anjilvel, S. (1995). The Effect of Fiber Inertia on Its Orientation in a Shear Flow with Application to Lung Dosimetry. *Aerosol Science and Technology*, 23(3):282–290.

Asgharian, B. and Yu, C. P. (1989). A Simplified Model of Interceptional Deposition of Fibers at Airway Bifurcations. *Aerosol Science and Technology*, 11(1):80–88.

Balásházy, I. (1994). Simulation of Particle Trajectories in Bifurcating Tubes. *Journal of Computational Physics*, 110(1):11–22.

Balásházy, I., Alföldy, B., Molnár, A. J., Hofmann, W., Szoke, I., and Kis, E. (2007). Aerosol Drug Delivery Optimization by Computational Methods for the Characterization of Total and Regional Deposition of

Therapeutic Aerosols in the Respiratory System. *Current Computer-Aided Drug Design*, 3(1):13–32.

Balásházy, I., Heistracher, T., and Hofmann, W. (1996). Air Flow and Particle Deposition Patterns in Bronchial Airway Bifurcations : The Effect of Different CFD Models and Bifurcation. *Journal of Aerosol Medicine*, 9(3):287–301.

Balásházy, I. and Hofmann, W. (1993). Particle deposition in airway bifurcations-I. Inspiratory flow. *Journal of Aerosol Science*, 24(6):745–772.

Balásházy, I., Martonen, T. B., and Hofmann, W. (1990). Fiber Deposition in Airway Bifurcations. *Journal of Aerosol Medicine*, 3(4):243–260.

Bar, J., Herbst, R. S., and Onn, A. (2009). Targeted drug delivery strategies to treat lung metastasis. *Expert Opinion on drug delivery*, 6(10):1003–1016.

Broday, D., Fichman, M., Shapiro, M., and Gutfinger, C. (1998). Motion of spheroidal particles in vertical shear flows. *Physics of Fluids*, 10(1):86.

Cai, F. S. and Yu, C. P. (1988). Inertial and Interceptional Deposition of Spherical Particles and Fibers in a Bifurcating Airway. *Journal of Aerosol Science*, 19(6):679–688.

Celik, I., Ghia, U., Roache, P., and Freitas, C. (2008). Procedure for Estimation and Reporting of Uncertainty Due to Discretization in CFD Applications. *Journal of Fluids Engineering*, 130(July):128–131.

Chan, T. L. and Yu, C. P. (1982). Charge Effects on Particle Deposition in the Human Tracheobronchial Tree. *Annual Occupational Hygiene*, 36(1):65–76.

Choi, L. T., Tu, J. Y., and Li, H. F. (2007). Flow and Particle Deposition Patterns in a Realistic Human Double Bifurcation Airway Model. *Inhalation Toxicology*, 19:117–131.

Dames, P., Gleich, B., Flemmer, A., Hajek, K., Seidl, N., Wiekhorst, F., Eberbeck, D., Bittmann, I., Bergemann, C., Weyh, T., Trahms, L., Rosenecker, J., and Rudolph, C. (2007). Targeted delivery of magnetic aerosol droplets to the lung. *Nature nanotechnology*, 2(8):495–9.

De Backer, J. W., Vos, W. G., Gorlé, C. D., Germonpré, P., Partoens, B., Wuyts, F. L., Parizel, P. M., and De Backer, W. (2008). Flow analyses in the lower airways: patient-specific model and boundary conditions. *Medical engineering and physics*, 30(7):872–9.

Dechaume, A., Finlay, W. H., and Minev, P. D. (2010). A two-grid fictitious domain method for direct simulation of flows involving particles of a very small size. *International Journal for Numerical Methods in Fluids*, 63(11):1241–1255.

Diaz-Goano, C., Minev, P. D., and Nandakumar, K. (2003). A fictitious domain/finite element method for particulate flows. *Journal of Computational Physics*, 192:105–123.

Ding, Y. J., Lieber, B., and Yu, C. P. (1993). Motion of a Fiber in a Bifurcating Tube Flow. *Aerosol Science and Technology*, 18(1):100–103.

Finlay, W. H. (2001). *The Mechanics of Inhaled Pharmaceutical Aerosols: An Introduction*. Academic Press, London.

Finlay, W. H., Lange, C. F., King, M., and Speert, D. P. (2000). Lung

Delivery of Aerosolized Dextran. *American journal of respiratory and critical care medicine*, 161:91–97.

Frey, P. and George, P. L. (2000). *Mesh Generation: application to finite elements*. Hermes Science, Lyons, 1st edition.

Gagnadoux, F., Pape, A. L., Lemarié, E., Lerondel, S., Valo, I., Leblond, V., Racineux, J.-L., and Urban, T. (2005). Aerosol delivery of chemotherapy in an orthotopic model of lung cancer. *The European respiratory journal*, 26(4):657–661.

Geuzaine, C. and Remacle, J. F. (2009). Gmsh: A 3-D finite element mesh generator with built-in pre- and post-processing facilities. *International Journal for Numerical Methods in Engineering*, 79(11):1309–1331.

Glowinski, R., Pan, T., Hesla, T. I., and Joseph, D. D. (1999). A distributed Lagrange multiplier/fictitious domain method for particulate flows. *International Journal of Multiphase Flow*, 25:755–794.

Golshahi, L., Seed, K. D., Dennis, J. J., and Finlay, W. H. (2008). Toward Modern Inhalational Bacteriophage Therapy: Nebulization of Bacteriophages of Burkholderia Cepacia Complex. *Journal of aerosol medicine and pulmonary drug delivery*, 21(4):351–359.

Guermond, J. L., Minev, P. D., and Shen, J. (2006). An overview of projection methods for incompressible flows. *Computer Methods in Applied Mechanics and Engineering*, 195:6011–6045.

Haefeli-bleuer, B. and Weibel, E. R. (1988). Morphometry of the Human Pulmonary Acinus. *The Anatomical Record*, 220:401–414.

Happel, J. and Brenner, H. (1965). *Low Reynolds Number Hydrodynamics*. Prentice-Hall, Englewood Cliffs.

Harris, R. L. and Fraser, D. A. (1976). A model for deposition of fibers in the human respiratory system. *American Industrial Hygiene Association Journal*, 37(2):73–89.

Hegedűs, C. J., Balásházy, I., and Farkas, A. (2004). Detailed mathematical description of the geometry of airway bifurcations. *Respiratory Physiology & Neurobiology*, 141:99–114.

Heistracher, T. and Hofmann, W. (1995). Physiologically Realistic Models of Bronchial Airway Bifurcations. *Journal of Aerosol Science*, 26(3):497–509.

Heyder, J. and Gebhart, J. (1977). Gravitational deposition of particles from laminar aerosol flow through inclined circular tubes. *Journal of Aerosol Science*, 8(4):289–295.

Hofmann, W., Balásházy, I., Moustafa, M., Szöke, R., El-Hussein, A., and Ahme, A. R. (2005). Simulation of Fiber Deposition in Bronchial Airways. *Inhalation Toxicology*, 17(13):717–727.

Horsefield, K., Dart, G., Olson, D. E., Filley, G. E., and Cumming, G. (1971). Models of the human bronchial tree. *Journal of Applied Physiology*, 31(2):207–217.

Jeffery, G. B. (1922). The Motion of Ellipsoidal Particles Immersed in a Viscous Fluid. *Proceedings of the Royal Society of London. Series A, Containing Papers of a Mathematical and Physical Character*, 102(715):161–179.

Kleinstreuer, C., Zhang, Z., and Donohue, J. F. (2008). Targeted Drug-Aerosol Delivery in the Human Respiratory System. *Annual Review of Biomedical Engineering*, 10:195–220.

KR, G. (1928). Zur Theorie der Brownschen Molekularbewe- gung. *Annalen der Physik*, 391:628–656.

Longest, P. W. and Vinchurkar, S. (2007). Effects of mesh style and grid convergence on particle deposition in bifurcating airway models with comparisons to experimental data. *Medical Engineering and Physics*, 29:350–366.

Martin, A. R. and Finlay, W. H. (2008a). Alignment of Magnetite-Loaded High Aspect Ratio Aerosol Drug Particles with Magnetic Fields. *Aerosol Science and Technology*, 42(4):295–298.

Martin, A. R. and Finlay, W. H. (2008b). Enhanced deposition of high aspect ratio aerosols in small airway bifurcations using magnetic field alignment. *Journal of Aerosol Science*, 39:679 – 690.

Martin, A. R. and Finlay, W. H. (2008c). Magnetic Alignment of Aerosol Particles for Targeted Pulmonary Drug Delivery: Comparison of Magnetic and Aerodynamic Torques. *Journal of Computational and Theoretical Nanoscience*, 5(10):2067–2070.

Myojo, T. (1990). The effect of length and diameter on the deposition of fibrous aerosol in a model lung bifurcation. *Journal of Aerosol Science*, 21(5):651–659.

Olson, D. E. and Hammersley, J. R. (1992). Physical models of the smaller pulmonary airways. *Journal of Applied Physiology*, 72(6):2402–2414.

Oseen, C. W. (1927). *Neuere Methoden und Ergebnisse in der Hydrodynamik*. Leipzig.

Otterson, G. A., Villalona-Calero, M. A., Sharma, S., Kris, M. G., Imondi, A., Gerber, M., White, D. A., Ratain, M. J., Schiller, J. H., Sandler, A., Kraut, M., Mani, S., and Murren, J. R. (2007). Phase I study of inhaled Doxorubicin for patients with metastatic tumors to the lungs. *Clinical cancer research : an official journal of the American Association for Cancer Research*, 13(4):1246–1252.

Phillips, C. G., Kaye, S. R., and Schroter, R. C. (1994). A diameter-based reconstruction of the branching patterns of the human bronchial tree. *Respiration physiology*, 98:193–217.

Reddy, L. H. and Couvreur, P. (2008). Novel Approaches to Deliver Gemcitabine to Cancers. *Current Pharmaceutical Design*, 14:1124–1137.

Redman, G. E. S., Martin, A. R., Waszak, P., Thompson, R. B., Cheung, P., and Finlay, W. H. (2010). Pilot study of inhaled aerosols targeted via magnetic alignment of high aspect ratio particles in rabbits. *Journal of Nanomaterials*, Accepted.

Roshchenko, A., Finlay, W. H., and Minev, P. (2011a). The Aerodynamic Behaviour of Fibers in a Linear Shear Flow. *Aerosol Science & Technology*, 45(10):1260–1271.

Roshchenko, A., Finlay, W. H., and Minev, P. (2011b). The Aerodynamic

Behaviour of Fibers in a Linear Shear The Aerodynamic Behaviour of Fibers in a Linear Shear Flow. *Aerosol Science & Technology*.

Shine, A. D. and Armstrong, R. C. (1987). The rotation of a suspended axisymmetric ellipsoid in a magnetic field. *Rheologica Acta*, 26:152–161.

Skomski, R., Hadjipanayis, G. C., and Sellmyer, D. J. (2007). Effective Demagnetizing Factors of Complicated Particle Mixtures. *IEEE Transactions on Magnetics*, 43(6):2956–2958.

Sturm, R. and Hofmann, W. (2009). A theoretical approach to the deposition and clearance of fibers with variable size in the human respiratory tract. *Journal of hazardous materials*, 170(1):210–8.

Subramanian, G. and Koch, D. L. (2005). Inertial effects on fibre motion in simple shear flow. *Journal of Fluid Mechanics*, 535:383–414.

Veeramani, C., Minev, P., and Nandakumar, K. (2007). A fictitious domain formulation for flows with rigid particles: A non-Lagrange multiplier version. *Journal of Computational Physics*, 224(2):867–879.

Weibel, E. R. (1963). *Morphometry of the Human Lung*. Academic Press, New York.

Wiedmann, T. S. and Yi, D. (2010). Inhalation Adjuvant Therapy for Lung Cancer. *Journal of aerosol medicine and pulmonary drug delivery*, 23(4):181–187.

Wittgen, B. P. H., Kunst, P. W. A., van der Born, K., van Wijk, A. W., Perkins, W., Pilkiewicz, F. G., Perez-Soler, R., Nicholson, S., Peters, G. J., and Postmus, P. E. (2007). Phase I study of aerosolized SLIT cisplatin in

the treatment of patients with carcinoma of the lung. *Clinical cancer research : an official journal of the American Association for Cancer Research*, 13(8):2414–2421.

Yu, C., Asgharian, B., and Yen, B. (1986). Impaction and Sedimentation Deposition of Fibers in Airways. *American Industrial Hygiene Association Journal*, 47(2):72–77.

Zhang, L., Asgharian, B., and Anjilvel, S. (1996). Inertial and Interceptional Deposition of Fibers in a Bifurcating Airway. *Journal of Aerosol Medicine*, 9(3):419–430.

Zhang, Z. and Kleinstreuer, C. (2001). Effect of Particle Inlet Distributions on Deposition in a Triple Bifurcation Lung Airway Model. *Journal of Aerosol Medicine*, 14(1):13–29.

Appendix A

Double Bifurcation

Before completing the single bifurcation steady flow analysis with the single bifurcation model several simulations were completed using a double bifurcation model. This was completed to validate the inlet condition on the single bifurcation model. Since the lung is a series of bifurcations it was important to ensure that that there were no flow patterns being missed by not including an upstream bifurcation in our deposition analysis. This section shows the results of a steady flow analysis on two different double bifurcation models.

A.1 Method

This section outlines the procedure used to simulate the steady air flow through a morphologically realistic double bifurcation using the fictitious domain algorithm.

A.1.1 Geometry Generation

Symmetric double bifurcation models were generated to represent two successive airways that would be found in generations 13-14-15 of the human lung. One model represents the situation when the all the parent and daughter branches

are in the same plane. The second model represents the situation when the first airway is located at a 90 degree plane to the daughter airway. Both models can be seen in Figure A.1. The length and diameter dimension for both models did not differ and were based on the symmetric lung geometry given by Hegedűs et al. (2004). All the dimensional parameters of the models are summarized in Table A.1 below.

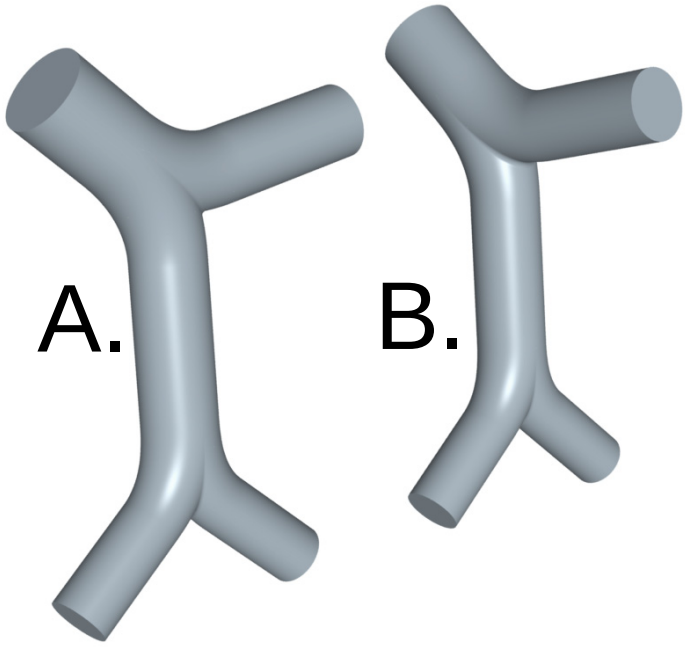

Figure A.1: Double bifurcation geometry **A.** Parent and daughter in same vertical plane **B.** Parent and daughter in in a 90 degree plane

Table A.1: Summary of double bifurcation dimensions in mm

	D_p	D_d	L_p	L_d	R^*	R_c	ϕ
Generation 13	0.73	0.61	0.73	0.62	1.22	0.061	50^o
Generation 14	0.61	0.49	0.62	0.92	0.98	0.049	50^o

A.1.2 Inlet Boundary Conditions

The inlet boundary conditions were based on the flow conditions found in generation 13 of a human lung during typical tidal breathing. The flow rate through the trachea of 18 l/min corresponds to typical tidal breathing of an adult male breathing through an aerosol delivery device with a mouthpiece. With the symmetrical branching model, the trachea flow rate results in a maximum velocity of 174.99 mm/s at the generation 13 bifurcation inlet. The inlet velocity profile was based on the condition that the flow is fully developed and laminar. To satisfy this condition, the Reynolds number and distance downstream must satisfy the following equations.

$$Re \leq 2300 \tag{A.1}$$

$$\frac{x}{D} > 0.06Re \tag{A.2}$$

The Reynolds number of 8.14 at the parent inlet and the geometry dimensions used in this study satisfy both A.1 and A.2. Thus the inlet boundary condition shown previously for the single bifurcation as Equation 3.15 is reasonable.

A.1.3 Outlet Boundary Conditions

For the double bifurcation model two different types of boundary had to be implemented to realistically simulate the flow patterns. The boundary conditions placed on the generation 14 daughter outlets are described by Equation (3.16) and Equation (3.17) for the velocity and pressure respectively.

For the daughter outlet belonging to generation 13 the above conditions could not be used. Applying the above boundary conditions would result in asymmetric flow through generation 13 due to the difference in pressure at the outlet of the gen 13 daughter and the straight portion between gen 13 and 14. Another daughter bifurcation was not added to the second generation 13 to decrease the already expensive computational work. There was also no available way to accurately calculate the pressure drop through the generation 13 bifurcation. Instead the velocity at the generation 13 daughter outlet was prescribed to a Poiseuille flow condition as expressed by Equation 3.15. V_{max} was based on a even division of the parent flow rate into two daughter tubes. This condition, though abnormal, gave the symmetric flow expected in a symmetric bifurcation and the straight outlet portion is long enough to not affect the flow condition experience between generation 13 and 14.

A.1.4 Bifurcation Wall Boundary Condition

The bifurcation wall was prescribed a no-slip boundary condition. Thus every node belonging to the wall boundary was given the condition described by Equation (3.18) in Section 3.4.4.

A.1.5 Flow Pattern Analysis

The main goal of this study was to gauge how the upstream bifurcation can affect both flow pattern at the inlet of the daughter bifurcation and also see if the upstream bifurcation affects secondary flow patterns (if any). An open source visualization program, PARAVIEW was used to visualize the flow. The velocity profile at the inlet of the daughter bifurcation was visualized to

ensure that it corresponded to a Poiseuille velocity profile.

To gauge the presence of secondary flow in the bifurcation, a secondary motion intensity factor (SMIF) was defined as the ratio between the local radial velocity and the average velocity inlet velocity of the parent branch (Heistracher and Hofmann, 1995). The SMIF was calculated and visualized throughout the bifurcation and the maximum was recorded. The SMIF values used in a comparison with the SMIF values of the single bifurcation flow analysis study described in the next section.

A.2 Double Bifurcation Steady Flow Results

Figure A.2 shows the velocity profile at the cross section where the single generation 14-15 single bifurcation would begin. On the same figure is the velocity profile for both the in plane and out of plane model. The maximum velocity found was found to be 125.91 m/s and 126.22 m/s for the in plane and out of plane bifurcation respectively. The SMIF value was found to be less than 0.1 in both the x and z direction except for very near the carina. The SMIF magnitude and values within the generation 14-15 bifurcation did not change significantly between the in plane and out of plane model.

A.3 Discussion

The goal of this section was to ensure that the single bifurcation flow conditions were accurate in representing the flow through a real bifurcation that is downstream of other bifurcations. The velocity through the straight section of the first generation was found to follow a Poiseuille flow as expected. This verifies the initial and boundary condition used at the inlet of the single

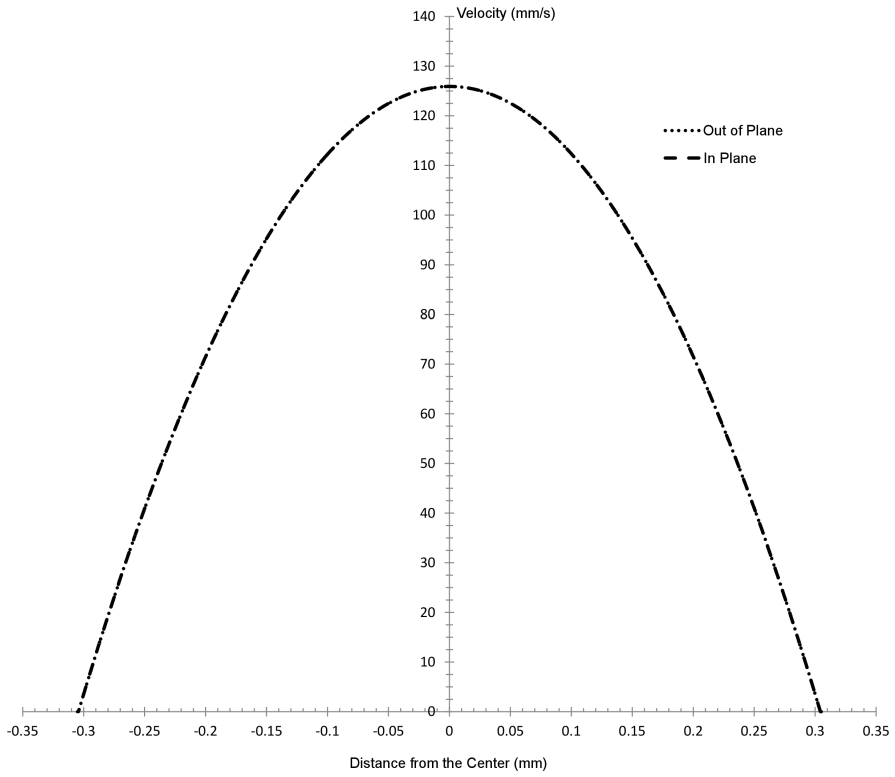

Figure A.2: Double bifurcation velocity profile at the inlet of the single bifurcation

bifurcation. Ensuring that the SMIF is below 0.1 means that there are no significant secondary flows within the bifurcation that could affect the particle trajectories. Since the secondary flow would not affect the particle trajectory this validates the no mixing assumption that is needed for the deposition calculations. The in and out of plane double bifurcation results allow for the use of the single bifurcation model with confidence since the flow is not affected by the upstream bifurcation.

Appendix B

Spherical Particle Validation

Before this study, the fictitious domain method (FDM) had never been used to simulate deposition of particles within a lung bifurcation. The goal of this section was to compare the trajectory of spherical particle when simulated using the FDM algorithm to results of a conventiona and widely accepted CFD program.

B.1 Method

This section describes the method taken to complete an analysis of the trajectory of a spherical particle in a single bifurcation. The bifurcation model and flow conditions used were the same as those used in the study with the FDM algorithm for a ellipsoid particle (See Section 3.4.1). This section introduces some new conditions associated with CFX, the CFD program used.

B.1.1 Bifurcation Geometry and Mesh Generation

The single bifurcation model used for this component of the study is the same morphologically realistic bifurcation model described in Section 3.2. For all

relevant geometrical parameters refer to Section 3.1.

The model was imported into the CFX Mesh program, where the grid was created. An unstructured tetrahedral mesh combined with an inflated boundary along the boundary of the bifurcation. The inflated boundary creates prism like mesh elements aligned with the flow near the bifurcation wall, where the velocity gradient is the highest. Elements sizes were chosen to produce a similar number of elements as the macro grid used for the fictitious domain algorithm.

B.1.2 CFX Solver

CFX-5 solves the particle transport equations corresponding to all three x, y and z momentum as a post processing step. To solve these equations a particle drag force option must be chosen. For sparsely distributed solid particles CFX gives the option of using the Schiller Naumann drag model. The following equations is used to calculate the coefficient of the drag force experienced by the particle

$$C_D = MAX\left(\frac{24}{Re}(1 + 0.15Re^{0.687}), 0.44\right) \tag{B.1}$$

The maximum value of the drag coefficient is based the constant drag force experienced by a spherical particle with a Reynolds number between 1000 and 200000.

B.1.3 Flow and Boundary Conditions

The fluid properties and flow conditions used for this component of the study correspond to the same values prescribed in the FDM simulations.

The inlet was prescribed a Poiseuille velocity profile described previously by Equation 3.15.

The particle injection points at the inlet were prescribed by using the injection with a user defined weighting option given by CFX. With this option the face weighting factor, W, at the inlet was calculated using Equation B.2

$$W = 1 - \frac{r^2}{R_p^2} \tag{B.2}$$

This equation prescribes a particle distribution profile that corresponds to the particle mass flow rate particle distribution along the inlet. This type of profile was also shown to match experimental results well by Zhang and Kleinstreuer (2001). In combination with the prescribed weighting distribution CFX also gives the option to either randomly place injection points or equally space the particles injection points. With the number of particles injected there was no real difference between either the random or equally space option and thus equally spaced particle injection was chosen.

The conditions placed on the outlet boundaries by CFX correspond to the same boundary conditions placed on the outlets in the FDM simulations. Equation 3.16 and Equation 3.17 previously given describe the conditions placed on the velocity and pressure at the outlets.

The fluid boundary condition at the bifurcation wall was prescribed as a no slip condition. Both the parallel and perpendicular restitution coefficient was given a value of zero so that particle would stick to the wall.

B.1.4 Convergence Criteria

Simulations results were considered converged once the number of particles deposited on the bifurcation wall no longer changed. This corresponded to the RMS and MAX particle momentum residual values of less than 1e-7 . The fluid momentum RMS and MAX residual values were also required to be below 1e-7 .

B.1.5 Effect of Particle Time Step on Deposition

The maximum integration time step of the particle trajectory calculation can be explicitly given in CFX. The maximum integration time step was systematically decreased by a magnitude of 10 and the change in deposition efficiency was recorded. To achieve a deposition efficiency change by less than 0.01%, a maximum integration time step of 1e-7 was used. This time step was then used for all the other simulations using CFX.

B.1.6 Mesh Convergence of Deposition

Due to the CFX not injecting the particles at the same exact positions for each simulation the actual particle trajectory between the refined and coarse mesh could not be compared. Instead the deposition efficiency was calculated using both the coarse and refined mesh to gauge the effect of the mesh size on the particle trajectories.

B.1.7 CFX Validation of FDM Code

To compare to the FDM particle trajectories were extracted from simulation done using the refined mesh and an integration time step of 1e-7. The

extracted particle trajectory from the CFX results was then compared to a FDM simulation of a particle being injected at the identical position as the CFX result.

B.2 Results

B.2.1 Effect of Time Step and Grid

The effect of the time step was recorded for both the coarse and refined grid. Table 2 shows the change in "regional" deposition of both grids with change in time step. The phrase "regional" deposition was used here because the inlet position of the particles was limited to a rectangular region stretching across the inlet and in line with the flow. This was done to ensure more deposition of particles when compared to the parabolic particle inlet profile. Since the trajectory of particles that deposit was the main interest, there was no need to simulate particles near the outside wall that will not deposit.

Table B.1: The relationship between the "regional" deposition and time step for both the coarse and refined grid. Also given is the absolute and relative difference between the results given by the coarse and refined grid.

Time Step (seconds)	Coarse Grid Deposition Efficiency (%)	Refined Grid Deposition Efficiency (%)	Relative Difference (%)
1.0e-3	6.920	6.491	3.10
1.0e-4	6.245	6.126	1.94
1.0e-5	5.331	5.826	0.85
1.0e-6	5.207	5.182	0.48
1.0e-7	5.198	5.176	0.43

The regional deposition decreased with time step in both the coarse and refined grid. The relative and absolute difference between the two grids also decreased with time step.

B.2.2 Spherical Particle Trajectory Comparison Between the CFX and FDM Result

The table below summarizes the differences between the final position of the CFX and the fictitious domain results. The first initial position tested corresponds to the center of the inlet and the second position is near the outer wall of the inlet. Table B.2 and Table B.3 correspond to the first and second inlet injection position respectively.

Table B.2: Final position results using CFX and the fictitious domain method (FDM). The initial position of the spherical particle was x = 2.20E-5 and z = 1.26E-3.

	Final Position (mm)			Absolute Difference (mm)			Magnitude
	x	y	z	x	y	z	(mm)
CFX	0.0884	-0.8440	0.0004	0.0417	-0.0388	-0.0004	0.0570
FDM	0.1301	-0.8829	0				

Table B.3: Final position results using CFX and the fictitious domain method. The initial position of the spherical particle was x = 2.40E-5 and z = 2.45E-3.

	Final Position (mm)			Absolute Difference (mm)			Magnitude
	x	y	z	x	y	z	(mm)
CFX	0.0649	-0.7941	0.0943	0.0168	-0.0166	-0.0011	0.0237
FDM	0.0815	-0.8109	0.932				

B.3 Discussion

The steady flow through the three dimensional bifurcation was successfully using the CFD program, CFX. The sensitivity analysis of the bifurcation grid found that the refined grid produced an acceptable convergence for the deposition. The sensitivity analysis also resulted in a suitable time step to use for the spherical trajectory simulations. This was completed to ensure

confidence in the accuracy of the CFX model.

The FDM trajectories and deposition points agreed with that of the CFX simulations. The difference between the results was less than 5% of the daughter length. The FDM results were also consistently found to deposit farther downstream when compared to the CFX result. This may be explained by considering that the CFX particle simulations do not account for the effects of the bifurcation wall. Utilizing a low Reynolds approach, Happel and Brenner (1965) studied a sphere moving perpendicular to a rigid plane wall, With the constraint that the sphere radius is small compared to the gap between the sphere and plane. For this case the drag force on the particle is given as

$$F_{dragnearwall} = 6\pi\mu U r_p \lambda \tag{B.3}$$

Here λ is a correction to the normal drag equation and is a function of sphere radius and gap width ratio. The expression for λ is not straight forward enough to solve without using a simple numerical approach but Happel and Brenner (1965) do give a table with values of λ for various values of the sphere radius and gap width ratio. For a gap width ratio of 1.12 and 6.1 the corresponding λ values are 9.25 and 1.12 respectively. So within 5 particle radii the drag force increases and thus the settling velocity would decrease due to the wall. This would explain why the FDM results show a decrease in the settling velocity when compared to the regular settling velocity. This also explains why the FDM results tended to deposit farther downstream when compared to the CFX results. In conclusion these results verify that the FDM algorithm is capable of accurately simulating the trajectory of a

particle through a three dimensional bifurcation model.